Materials Chemistry and Physics 362 (2026) 132752

Contents lists available at ScienceDirect

Materials Chemistry and Physics

journal homepage: www.elsevier.com/locate/matchemphys

Electrodeposition growth of multiphase metal telluride thin films: Structural, optical, electrical properties, and DFT calculations

Panupat Chaiworn [a], Pensri Pramukkul [a], Prayoonsak Pluengphon [b], Ekasiddh Wongrat [c], Phathaitep Raksa [d], Piyanooch Nedkun [e], Auttasit Tubtimtae [f,*]

[a] Department of Physics and General Science, Chiang Mai Rajabhat University, Mae Rim, Chiang Mai, 50180, Thailand
[b] Division of Physical Science, Faculty of Science and Technology, Huachiew Chalermprakiet University, Samutprakarn, 10540, Thailand
[c] School of Science, University of Phayao, Phayao, 56000, Thailand
[d] Department of Applied Physics, Faculty of Science and Liberal Arts, Rajamangala University of Technology Isan, Nakhon Ratchasima, 30000, Thailand
[e] General Science Department, Faculty of Science and Engineering, Kasetsart University Chalermphrakiet Sakon Nakhon Province Campus, Sakon Nakhon, 47000, Thailand
[f] Division of Physics, Department of Physical and Material Sciences, Faculty of Liberal Arts and Science, Kasetsart University Kamphaeng Saen Campus, Nakhon Pathom, 73140, Thailand

HIGHLIGHTS

- The effects of applied electrodeposition potentials were investigated for multiphase metal telluride thin films.
- Recrystallization and phase transformation processes driven by energy stored in the parent Bi_2Te_3 phase.
- The band gap decreased from 3.75 to 1.52 eV with increasing electrodeposition potential.
- A significant decline in E_{ac} was observed between 6 and 8 V due to enhanced thermally-activated conduction.
- Bi_2Te_3 and Sb_2Te_3 exhibited higher absorption coefficient than Al_2Te_3 and Al_7Te_{10}.

ARTICLE INFO

Keywords:
Electrodeposition
Metal telluride thin films
Multiphase systems
Sb/al doping
Photoabsorption coefficient

ABSTRACT

This study investigated the effects of applied electrodeposition potentials on the structural, optical, and electrical properties of multiphase metal telluride thin films for optoelectronic applications. The rhombohedral Sb_2Te_3, Bi_2Te_3, Al_7Te_{10}, and Bi_4Te_3 phases were identified and incorporated into thin films containing hexagonal Bi_2Te, BiTe, and monoclinic Al_2Te_3. Variations in the crystallographic parameters are attributed to recrystallization and phase transformation processes driven by the energy stored in the parent Bi_2Te_3 phase. Scanning electron microscopy (SEM) images showed a compact inner surface covered with residuals dispersed across the film surface at the applied potentials of 4 and 6 V. At an applied potential of 8 V, crack formation accompanied by a reduction in surface residuals was observed, whereas films deposited at 10 V exhibited more pronounced cracking with no noticeable residuals. Energy-dispersive X-ray spectroscopy (EDS) confirmed the presence of Al, Sb, Te, and Bi in all the deposited films, indicating the successful incorporation of binary multiphase metal chalcogenide compounds. The band gaps of the deposited films are decreased with increasing electrodeposition potential, highlighting the tunability of the electronic properties of multiphase metal telluride thin films. A significant decline in the activation energy (E_{ac}) was observed between 6 and 8 V, suggesting that this range is the optimal applied voltage window for device applications due to enhanced thermally activated conduction. Finally, density functional theory (DFT) calculations of the photoabsorption coefficient indicated that Bi_2Te_3 and Sb_2Te_3 exhibited higher absorption coefficients than Al_2Te_3 and Al_7Te_{10}. Among these materials, Bi_2Te_3 exhibited the strongest absorption coefficient at higher photon energies, whereas the other phases exhibited enhanced absorption in the red-light region.

* Corresponding author.
E-mail address: tubtimtae@gmail.com (A. Tubtimtae).

https://doi.org/10.1016/j.matchemphys.2026.132752
Received 1 February 2026; Received in revised form 14 May 2026; Accepted 3 June 2026
Available online 4 June 2026

1. Introduction

Over the past decade, the field of photonics has experienced remarkable advancements, enabling a wide range of practical applications including telecommunications, imaging, and energy conversion. In this context, optical-material-based binary chalcogenide semiconductor thin films have attracted increasing attention. This growing interest has motivated researchers to investigate the optical properties of diverse materials, particularly with respect to their potential applications in energy-related technologies [1]. Previously, a wide range of metal chalcogenides, including CdS [2], CdSe [3], ZnS [4], PbSe [5], CdTe [6], Cu_2Te [7], and Sb_2S_3 [8], have been extensively investigated and shown to possess superior adjustable bandgap properties suitable for diverse applications. These applications include display devices, photodiodes, gas sensors, photosensors, solar cells, thermoelectric conversion devices, transparent electrodes, and photovoltaic devices [9]. Among these materials, bismuth telluride (Bi_2Te_3) has emerged as a particularly promising candidate owing to its unique topological insulator (TI) characteristics featuring topologically protected surface states and novel quantum states. These properties have attracted significant theoretical and experimental interest in condensed-matter physics [10], and have unique electronic properties relevant to spintronic applications [11]. However, to induce novel phenomena such as the quantum anomalous Hall effect, insulator materials must break time-reversal symmetry (TRS), which leads to the opening of an energy gap at the Dirac point [11]. While spin–momentum locking and the suppression of backscattering from nonmagnetic impurities are intrinsic features of topological surface states, TRS breaking is essential for realizing magnetically driven quantum transport phenomena [11]. In practice, TRS breaking is typically achieved by introducing a ferromagnetic order into the TI via transition-metal doping. This process induces an exchange interaction between the surface states and spontaneous magnetization, leading to the formation of a small exchange gap [11].

Single-element doping to form binary metal chalcogenide materials has been widely explored because of its ability to modify structural characteristics and improve optical and electrical properties. For example, Bibby et al. synthesized nanocrystalline Mn-doped Bi_2Te_3 thin films using magnetron sputtering. X-ray diffraction analysis revealed the incorporation of binary MnTe and $MnTe_2$ compounds within the thin films. The authors concluded that the prominence of MnTe phases in the deposited films suggests that further optimization of the growth parameters could enable the realization of $MnBi_2Te_4$ via magnetron sputtering [11]. In a related approach, M–K. Han et al. synthesized p-type Bi_2Te_3-based thermoelectric (TE) materials by intercalating and substituting Cr within Bi_2Te_3 layers, forming $Cr_xBi_2Te_3$ and $Cr_xBi_{2-x}Te_3$ compounds, respectively. The presence of a secondary Cr_2Te_3 phase was also identified in the XRD patterns, which led to a substantial increase in electrical conductivity and concurrent reduction in thermal conductivity [12]. Similarly, a binary $Cu_{2-x}Te$ phase was observed in Cu-doped Bi_2Te_3 thin films, leading to enhanced thermoelectric properties [13]. Furthermore, indium incorporation into the Bi_2Te_3 matrix promoted the formation of In_2Te_3 microstructural phases, which significantly influenced the thermoelectric transport properties. Thus, the reduction in lattice thermal conductivity, accompanied by decreased resistivity, was attributed to indium doping acting as an electron donor and high-pressure inhibition effects [14].

In this study, co-doping with Sb and Al was implemented for the first time in Bi_2Te_3 thin films synthesized via electrodeposition, leading to the formation of co-binary metal chalcogenide compounds within the deposited thin films. A range of deposition potentials were employed to investigate the resulting modifications in the structural, optical, and electrical properties, complemented by density functional theory (DFT) calculations. Owing to the smaller ionic radii of Sb^{3+} (0.76 Å) and Al^{3+} (0.535 Å) [15] compared with Bi^{3+} (1.03 Å) [16] and Te^{2-} (2.21 Å) [17], these dopants can substitute into the Bi_2Te_3 lattice with minimal lattice distortion, promoting good structural integration and a low density of crystal defects [18]. Sb^{3+} ions, with a $5s^2$ outer electronic configuration, have been widely introduced into semiconductor systems and have been shown to increase electrical conductivity while maintaining optical transparency in the visible region, thereby exhibiting strong potential for enhancing and tailoring the optical properties [19,20]. Thus, Sb plays a critical role in modifying the fundamental physical properties of numerous semiconductors for optoelectronic device applications [21]. Al^{3+} can act as an acceptor dopant, and its incorporation is often accompanied by the formation of oxygen vacancies that behave as donor defects. In addition, Al^{3+} is widely utilized in energy storage systems because it delivers a higher charge per unit ion than alternative cations during intercalation and de-intercalation processes [22]. Furthermore, the insertion of Al^{3+} ions is expected to increase the surface energy of the non-polar *m*- and *a*-planes, resulting in faster growth along these crystallographic directions [23]. This enhanced growth may facilitate the incorporation of specific point defects such as oxygen vacancies and interstitial dopants, leading to the formation of localized energy states. The presence of these states can provide additional pathways for electronic transitions, potentially enhancing light absorption within specific energy or wavelength ranges and enabling bandgap tuning via the Burstein–Moss (B-M) effect [24,25].

2. Experimental details

2.1. Solution preparation

Multiphase metal telluride thin films were synthesized via electrodeposition using a Bi_2Te_3-based precursor solution containing Bi and Te ions. A 0.05 M Bi_2Te_3 solution was prepared by dissolving Bi_2Te_3 powder in 50 mL of a methanol/deionized (DI) water mixture (7:3, v/v), followed by vigorous stirring for 10 min. For the introduction of Sb^{3+} cations, a 0.05 M $SbCl_3$ solution was prepared by dissolving $SbCl_3$ crystals in an ethanol/DI water mixture (7:3, v/v) and stirring for an additional 10 min. The two precursor solutions were then combined and vigorously stirred for 10 min to ensure homogeneity. All solution preparation steps were performed at ambient temperature.

2.2. Thin film preparation

Prior to thin-film growth, fluorine-doped tin oxide (FTO) glass substrates were subjected to a meticulous cleaning procedure to ensure high deposition quality [18]. The substrates were first immersed in a nitric acid/DI water solution (3:7, v/v) and ultrasonicated for 10 min. Subsequently, they were ultrasonically cleaned in acetone, methanol, and deionized (DI) water for 10 min each to remove residual contaminants. An aluminum plate was cut to 2.5 cm × 5 cm, polished using sandpaper, and thoroughly rinsed with DI water. Once the precursor solution, FTO substrates, and aluminum plate were prepared, electrodeposition was performed, as illustrated in Fig. 1. The aluminum plate and FTO glass substrate were connected to the positive and negative terminals of the power supply, serving as the anode and cathode, respectively, and immersed in the Bi_2Te_3 precursor solution. Electrodeposition was performed at the applied potentials of 4, 6, 8, and 10 V for 60 min. Following the deposition, the coated FTO substrates were annealed in an oven at 120 °C for 12 h. Finally, thin-film-coated FTO glass substrates corresponding to each applied deposition potential were obtained.

2.3. Characterization of multiphase metal chalcogenides

The crystallinity and structural phases of the thin films were characterized using an X-ray diffractometer (Rigaku Miniflex II) operated at 30 kV and 15 mA with Cu-Kα radiation (λ = 1.5406 Å). Diffraction patterns were recorded over a 2θ range of 10–60° with a step size of 0.01°. The surface morphologies and elemental compositions of the films were examined using an ultrahigh-resolution scanning electron microscope (UHR-SEM, TESCAN CLARA) equipped with an energy-

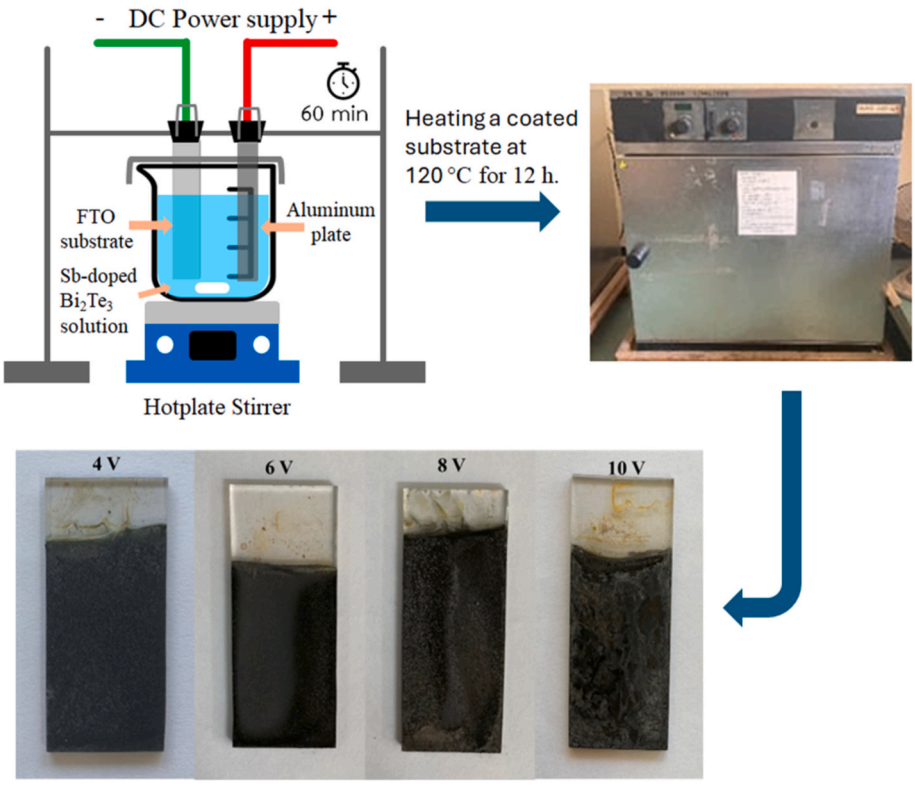

Fig. 1. Schematic diagram of thin film preparation using the electrodeposition method.

dispersive X-ray spectroscopy (EDS) system (Oxford Ultim® Max, 40 mm^2 detector). High-resolution atomic force microscopy (HR-AFM) with dynamic force mode (DFM) measurements (Seiko Instruments Nano-Technology, probe station: SPI3800 N, head unit: SPA-400) was used to examine the topographical characteristics of the sample surface in a scanning area of 10 × 10 μm^2 for each applied voltage potential.

X-ray photoelectron spectroscopy (XPS) measurements were conducted at the Thailand Center of Excellence in Physics on an AXIS Ultra DLD spectrometer (Kratos Analytical Ltd.) using a soft X-ray beam produced by monochromated Al Kα radiation ($h\nu$ = 1486.6 eV) under ultra-high vacuum (UHV) ($<10^{-7}$ Pa) with an anode voltage of 15 kV and an emission current of 20 mA (a power of 300 W). The survey spectra were detected with a constant analyzer energy of 80 eV at 1 eV intervals, while the high-energy resolution spectra were obtained with a constant analyzer energy of 20 eV at 0.1 eV intervals. All peaks are calibrated by the carbon deposit C 1s of C–C and C–H bonds in hydrocarbons at binding energy at 284.8 eV as standard to compensate for any charge-induced shifts [26].

Optical transmittance and reflectance measurements were performed at ambient temperature using a UV–Vis–near-infrared (NIR) spectrophotometer (Varian Cary 50 Conc.) over a wavelength range of 300–1000 nm.

The electrical properties were measured using a Keithley 6485 picoammeter, and the electrical resistance (R) was calculated as the ratio of the applied voltage to the measured current that determines the activation energy through temperature-dependent electrical resistance measurements, which were conducted over the range of 298.15–400.15 K. Further analysis of the electrical properties of the deposited multiphase metal telluride thin films, Van der Pauw Hall effect measurement system (Linseis, Model: L79/HCS) at room temperature was used to determine the sheet resistance/resistivity, carrier concentration, carrier type, and carrier mobility of the thin films using a four-point probe method.

3. Results and discussion

3.1. Structural properties and phase analysis

The XRD patterns of the multiphase metal-chalcogenide thin films are shown in Fig. 2. The diffraction patterns revealed that the films deposited at all applied electrodeposition potentials exhibited a polycrystalline structure. Crystallinity was qualitatively assessed based on the presence, sharpness, and intensity of the diffraction peaks. In the overall XRD patterns at each applied voltage, the prominent peaks exhibited lower sharpness, intense peaks indicated a lower degree of crystallinity, and broader peaks suggested reduced crystalline or partial amorphous character. In addition, quantitative or semiquantitative analyses of crystallinity can be performed by estimating the crystalline fraction. Diffraction peaks in Fig. 2 corresponding to the rhombohedral Sb_2Te_3 phase were observed at two θ positions, 17.13° to 17.14° and

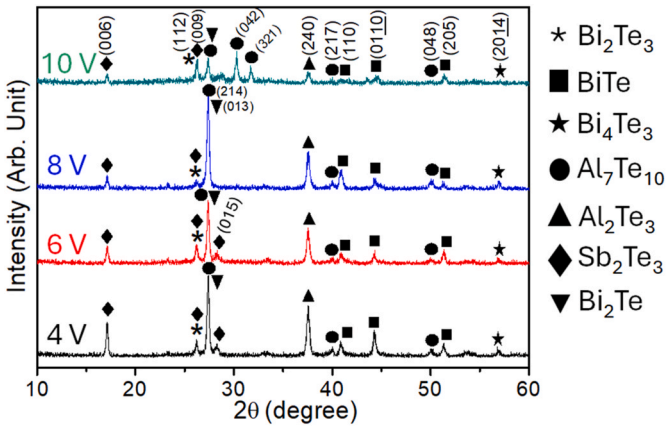

Fig. 2. X-ray diffraction patterns of multiphase metal chalcogenide thin films deposited at various electrodeposition potentials.

26.22° to 26.26°, which were indexed to the (006) and (009) planes, respectively (JCPDS file no. 00-015-0874). An additional reflection at the 2θ position of 28.25°–28.27°, indexed to the (015) plane of Sb_2Te_3, was detected in films deposited at 4 and 6 V; however, this peak disappeared at higher applied deposition potentials. Moreover, a diffraction peak at a similar 2θ position 26.22°–26.26°) was assigned to the (112) plane of the rhombohedral Bi_2Te_3 phase (JCPDS file no. 01-085-0439), which was present at all applied electrodeposition potentials.

A prominent diffraction peak at 2θ ≈ 27.38° was assigned to the (214) and (013) planes of the rhombohedral Al_7Te_{10} phase (JCPDS file no. 01-078-1492) and hexagonal Bi_2Te phase (JCPDS file no. 00-042-0540), respectively. Additional reflections corresponding to the rhombohedral Al_7Te_{10} structure were observed at ~40° and 50° and were indexed to the (217) and (048) planes. In addition, the presence of monoclinic Al_2Te_3 was confirmed by the diffraction peak appearing at 37.55°–37.59°, corresponding to the (240) crystal plane (JCPDS file no. 01-086-2013). The hexagonal BiTe phase was also identified, with diffraction peaks indexed to the (110) and (01$\underline{1}$0) crystal planes at 40.89°–40.92° and 44.29°–44.53°, respectively (JCPDS file no. 01-083-1749).

An additional hexagonal BiTe phase was identified by a diffraction peak at 2θ ≈ 51.31°–51.44°, which was indexed to the (205) crystal plane (JCPDS file no. 01-075-1095). Finally, reflections corresponding to the rhombohedral Bi_4Te_3 phase were observed at 2θ ≈ 56.89°–57.04° and indexed to the (2014) plane (JCPDS file no. 00-033-0216). The enhanced crystallinity of the thin films was evidenced by the high intensity and sharpness of the diffraction peaks corresponding to the rhombohedral Al_7Te_{10} and hexagonal Bi_2Te phases at an applied electrodeposition potential of 8 V, whereas a clear reduction in peak intensity and sharpness was observed at 10 V. Accordingly, the optimal peak definition at 8 V suggests potential improvements in the photovoltaic performance [27]. However, the low intensity of all XRD peaks at the highest applied potential of 10 V indicates the formation of a quasi-crystalline structure in the multiphase metal chalcogenide thin films.

The X-ray diffraction patterns obtained at higher applied electrodeposition potentials showed a slight shift of most diffraction peaks toward higher angles. This shift can be attributed to a decrease in the lattice parameters due to the substitution of smaller Sb^{3+} (0.76 Å) and Al^{3+} (0.535 Å) ions for larger Bi^{3+} (1.03 Å) and Te^{2-} (2.21 Å) ions within the crystal lattice. The corresponding interplanar spacing (d_{hkl}) can be calculated using Bragg's law [28].

$$d_{hkl} = \frac{n\lambda}{2\ sin\ \theta_{hkl}}, \quad (1)$$

where n is the order of diffraction (typically equal to 1), λ is the X-ray wavelength (1.5406 Å), and θ is the diffraction angle (Bragg angle). As summarized in Table 1, the reduction in d_{hkl} corresponds to an increase in the diffraction angle, which confirms the incorporation of Sb^{3+} and Al^{3+} ions into the Bi_2Te_3 lattice, and is associated with increased structural heterogeneity and lattice contraction at higher applied electrodeposition potentials [27,29]. However, the slight shifts toward higher diffraction angles indicate only minor alterations in the lattice parameters with increasing applied electrodeposition potential, suggesting that smaller ions are incorporated into the Bi_2Te_3 lattice without significantly disrupting the crystal structure or crystallinity. Thus, these small changes in interplanar spacing may generate localized strain and defect formation, including dislocations, within the thin films during growth. Moreover, the geometric mismatch at the interface between the crystal lattice of the metal chalcogenide thin films and the glass

Table 1
Structural parameters of multiphase of metal chalcogenide thin films synthesized by various electrodeposited potentials.

Applied potentials	Plane (*hkl*)	2θ (degree) (from fitting)	β (radian)	d_{hkl} (Å)	D_{ps} (nm)	ε ($\times10^{-3}$)	δ ($\times10^{-4}$ nm^{-2})
4 V	(006)	17.13	0.00422	5.172	42.79	1.24	5.46
	(112)/(009)	26.22	0.00361	3.396			
	(214)/(013)	27.38	0.00457	3.254			
	(240)	37.55	0.00611	2.393			
	(110)	40.89	0.00534	2.205			
	(01$\underline{1}$0)	44.29	0.00504	2.043			
	(048)	50.06	0.00676	1.820			
	(205)	51.31	0.00588	1.779			
	(20$\underline{1}$4)	56.89	0.00573	1.617			
6 V	(006)	17.14	0.00461	5.169	37.37	1.04	7.16
	(112)/(009)	26.23	0.00463	3.394			
	(214)/(013)	27.38	0.00464	3.254			
	(240)	37.55	0.00623	2.393			
	(110)	40.92	0.00491	2.203			
	(01$\underline{1}$0)	44.29	0.00484	2.043			
	(048)	50.04	0.00677	1.821			
	(205)	51.33	0.00599	1.778			
	(20$\underline{1}$4)	56.90	0.00660	1.617			
8 V	(006)	17.14	0.00449	5.169	37.99	1.44	6.93
	(112)/(009)	26.23	0.00503	3.394			
	(214)/(013)	27.38	0.00485	3.254			
	(240)	37.57	0.00604	2.392			
	(110)	40.92	0.00695	2.203			
	(01$\underline{1}$0)	44.33	0.00525	2.041			
	(048)	50.07	0.00880	1.820			
	(205)	51.31	0.00580	1.779			
	(20$\underline{1}$4)	56.92	0.00651	1.616			
10 V	(006)	17.13	0.00403	5.172	37.58	1.98	7.08
	(112)/(009)	26.26	0.00393	3.391			
	(214)/(013)	27.38	0.00482	3.254			
	(240)	37.59	0.00665	2.391			
	(110)	-	-	-			
	(01$\underline{1}$0)	44.53	0.01798	2.033			
	(048)	-	-	-			
	(205)	51.44	0.00627	1.775			
	(20$\underline{1}$4)	57.04	0.00276	1.613			

substrate is influenced by the applied electrodeposition potential [27].

The particle sizes (D_{ps}) were determined using the Williamson-Hall (W–H) method, which also provides indirect information about the crystalline nature of the material according to the following relation [30]:

$$\beta \cos\theta = 4\varepsilon \sin\theta + \frac{0.9\lambda}{D_{ps}} . \quad (2)$$

Here, β represents the full width at half maximum (FWHM) corresponding to the most intense peaks. The y-axis intercept and slope of the W–H plots of $\beta \cos\theta$ vs. $4 \sin\theta$, shown in Fig. 3(a–d) for metal chalcogenide thin films deposited at different applied electrodeposition potentials were used to determine the particle size (D_{ps}) and microstrain (ε), respectively. The D_{ps} values determined using the W–H method are summarized in Table 1 and were found to be 42.79, 37.37, 37.99, and 37.58 nm, while the ε values were 1.24×10^{-3}, 1.04×10^{-3}, 1.44×10^{-3}, and 1.98×10^{-3} with increasing applied electrodeposition potential.

Furthermore, to gain additional insight into the defect formation in multiphase metal chalcogenide thin films, the dislocation density (δ) was evaluated using Eq. (3) [18,27]:

$$\delta = \frac{1}{D^2} . \quad (3)$$

The δ values, also listed in Table 1, were found to be 5.46×10^{-4}, 7.16×10^{-4}, 6.93×10^{-4}, and 7.08×10^{-4} nm^{-2} for potentials of 4, 6, 8, and 10 V, respectively. All the structural parameters are summarized in Fig. 4, which shows an overall decrease in D_{ps} accompanied by increasing ε and δ values for applied potentials above 4 V, that is, from 6 to 10 V. These variations can be attributed to the recrystallization and phase transformation processes driven by the energy stored in the parent Bi_2Te_3 phase. The interplay between microstructural parameters, that is, grain boundaries, lattice strain, and dislocation density, may also influence the subsequent microstructural evolution during the electrodeposition process. In addition, the increase in the grain boundary length with decreasing particle size indicates that the dislocation density is

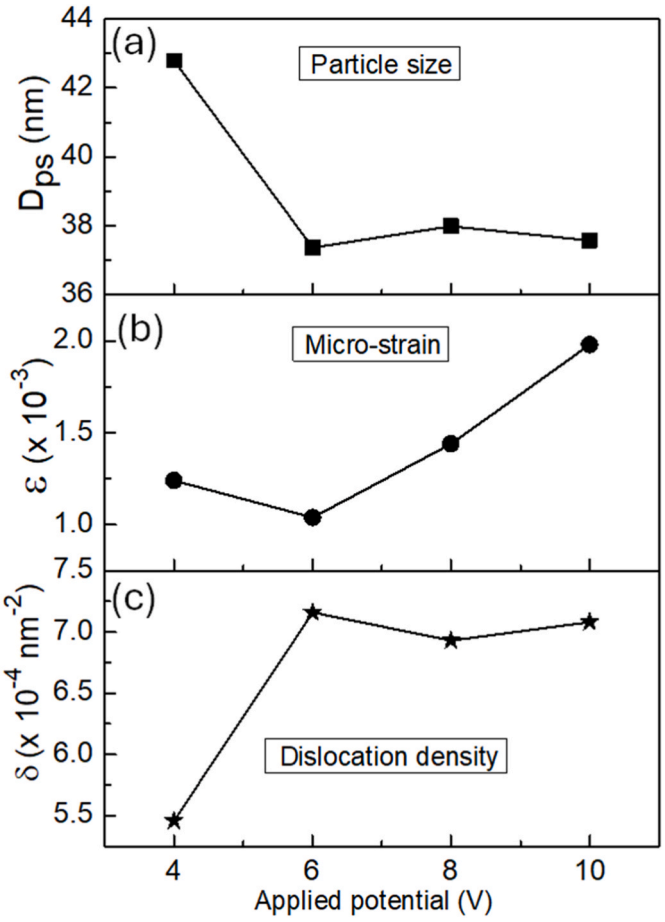

Fig. 4. Variation of structural parameters with electrodeposition potential: (a) particle size, (b) microstrain, and (c) dislocation density.

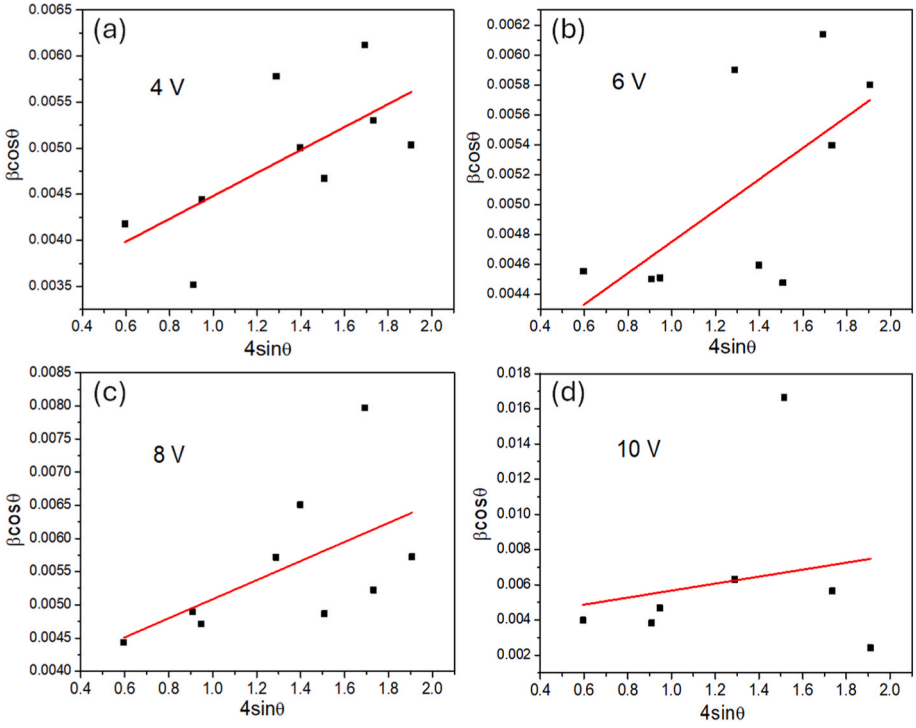

Fig. 3. Williamson-Hall (W–H) plots derived from the XRD patterns of the thin films deposited at various electrodeposition potentials.

predominantly governed by dislocation formation at the grain boundaries. The associated grain boundary energy acts as a driving force for the metastable to stable phase transformation in thin-film materials, showing that the phase transformation kinetics are a function of particle size. Therefore, these observations imply that the dislocation density in multiphase metal chalcogenide thin films is directly correlated with the boundary fraction, which is governed by particle size [31].

3.2. Morphological characteristics and elemental analysis

Fig. 5 shows the SEM images of multiphase metal chalcogenide thin films electrodeposited at different applied potentials. The images revealed significant potential-dependent differences in roughness, while the films remained free of cracks, voids, and pinholes. At the applied potentials of 4 and 6 V (Fig. 5(a–b)), the film surfaces were compact and covered by residuals dispersed across the surface. As the applied potential increased from 4 to 6 V, these residuals became more scattered and irregularly distributed [27]. Notably, at an applied potential of 8 V (Fig. 5(c)), the films exhibited the onset of surface cracking, accompanied by a noticeable reduction in the residuals. At 10 V (Fig. 5(d)), the crack formation became more pronounced, with the film surface largely devoid of residuals. The formation of cracks at higher applied potentials was attributed to the increased substitution of Sb^{3+} and Al^{3+} ions into the Bi_2Te_3 lattice. Owing to their smaller ionic radii relative to Bi^{3+} and Te^{2-} ions, this substitution induces lattice stress and local distortion, alters the surface energy balance, and ultimately modifies thin-film growth dynamics [32]. These morphological changes are consistent with the XRD results, which showed a reduced particle size at an applied potential of 10 V. Furthermore, the reduction in surface residuals might be due to their rearrangement into smaller nanoparticles, followed by incorporation into the growing thin film. The thicknesses of the thin films are shown in Fig. 6. The thin film deposited at an applied potential of 4 V exhibited a thickness of approximately 13 μm (Fig. 6(a)), which decreased to approximately 8 μm at 6 V (Fig. 6(b)). With further increases in the applied electrodeposition potential to 8 and 10 V, the film thickness was further reduced to approximately 5 μm, as shown in Fig. 6 (c and d), respectively.

As shown in Fig. 7(a–d), the thin films deposited at applied electrodeposition potentials ranging from 4 to 10 V consistently contained Al, Sb, Te, and Bi, confirming the successful incorporation of binary multiphase metal chalcogenide compounds within the films. The presence of Cl in the thin films could be attributed to the SbCl precursor. However, changes in the elemental composition were observed because of the diverse morphologies and surface variations in the multicompositional nature of the nanoparticles, which are directly associated with the coexistence of different phases and elemental compositions within the films [33], [34].

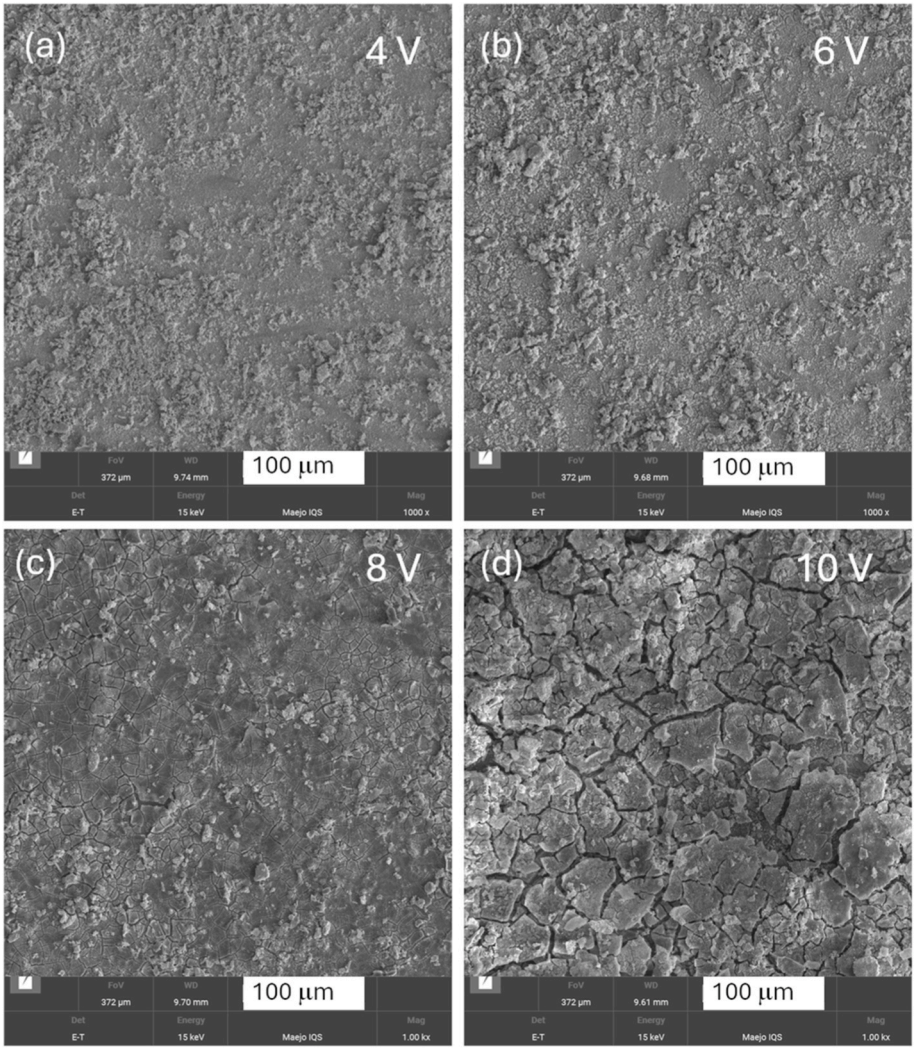

Fig. 5. Surface characteristics of multiphase metal chalcogenide thin films deposited at electrodeposition potentials of (a) 4V, (b) 6 V, (c) 8 V, and (d) 10 V.

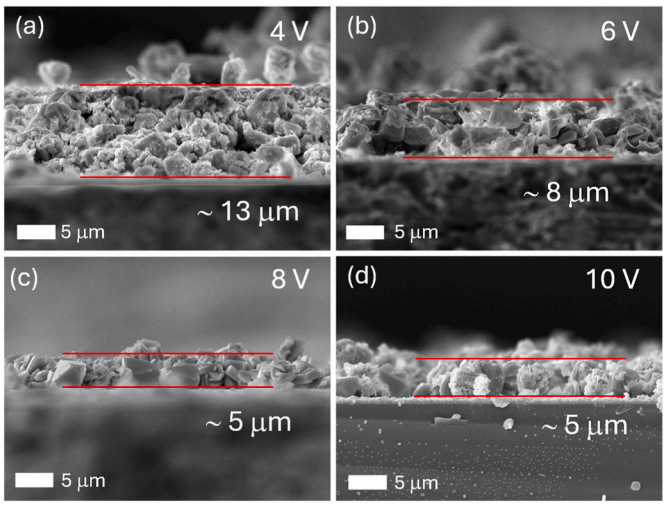

Fig. 6. Thickness of multiphase metal chalcogenide thin films deposited at electrodeposition potentials of (a) 4V, (b) 6 V, (c) 8 V, and (d) 10 V.

3.3. Topographical analysis

The topographical characteristics were analyzed using surface roughness parameters, including surface slope (S_{dq}), arithmetic mean roughness (S_a), root mean square roughness (S_q), and root mean square (RMS) values, derived from AFM, as shown in Fig. 8 and presented in Table 2.

The surface roughness parameters of the thin films with applied electrodeposited potentials from 6 to 8 V displayed a general increase in the surface slope (S_{dq}) and RMS values, indicating a progressive transformation and an escalation in surface roughness in this applied electrodeposited potential range [35]. As shown in Fig. 8(b), the thin film with an applied electrodeposited potential of 6 V exhibits an S_{dq} of 0.2784 and an RMS value of 24.1810 nm, which increases to 0.4154 and 34.9269 nm, respectively, for the thin film with an applied potential of 8 V, as observed in Fig. 8(c). A gradual change in the surface topography promotes defect generation, localized surface diffusion, and clustering in thin films [36]. Nevertheless, at an applied electrodeposited potential of 10 V, the S_{dq} and RMS values diminish, indicating a potential smoothing effect or an alternative partial surface restructuring/-reorganization mechanism with a reduction of residuals on the surface of the thin film, as shown in Fig. 8(d) [36], which are close to and slightly higher than those of the S_{dq} and RMS values for the thin film with an applied electrodeposited potential of 4 V in Fig. 8(a). The S_a value for the thin film of 6 V is 15.0136 nm, which notably increases to 20.7929 nm at an applied electrodeposited potential of 8 V. This implies that this electrodeposited potential range leads to a significant increase in surface roughness. A decline in the arithmetic mean roughness (S_a) of 16.2566 nm at an applied electrodeposited potential of 10 V indicated that the surface roughness tended to decrease when the applied electrodeposited potential exceeded 8 V. These findings suggest that a moderate applied voltage range increases the surface roughness through the creation of defects and changes in the surface morphology. However, at 10 V, the surface may undergo some reorganization or recovery processes, which results in reduced roughness. The alterations observed in the surface roughness and optical characteristics as a function of the applied voltage can be ascribed to the interactions occurring between the Sb^{3+}/Al^{3+} ion incorporation and the atomic configuration of the Bi–Te thin films.

At the applied electrodeposited potential of 8 V, this applied potential facilitates the introduction of ion incorporation, which induces localized defects within the mesoporous matrix of the thin film, thereby resulting in an elevation of the surface roughness, as verified by the AFM data in Table 2. As the applied electrodeposited potential increased to 10 V, these defects accumulated, causing additional disorder and modifying optical attributes, including an enhancement in the absorption coefficient and a reduced shift in the energy band gap. Consequently, the thin film may experience structural reorganization, culminating in a decrease in the surface roughness attributable to defects and atomic structure rearrangement. This reorganization stabilizes the optical properties and reinstates a certain degree of order on the surface, as evidenced by the observed reduction in roughness and modulation of optical parameters. Our results are similar to those of previous reports on the impact of proton ion irradiation on $Se_{70}Te_{20}Sn_{10}$ and $Se_{70}Te_{20}In_{10}$ thin films [35,37]. This behavior implies a dynamic stability between defect creation and the lattice recovery process in response to ion incorporation, which has significant implications for the potential utilization of these films in photonic and optoelectronic

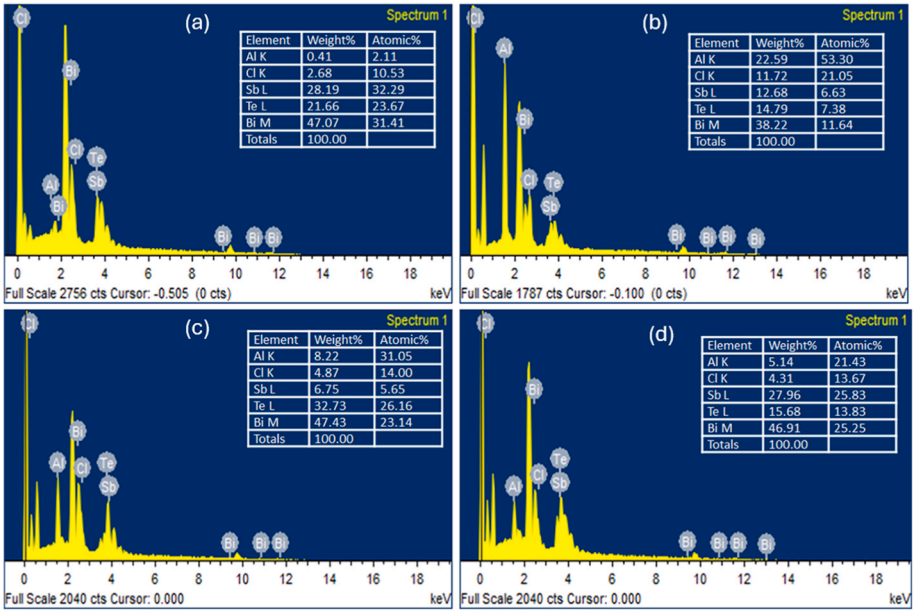

Fig. 7. EDS spectra showing the elemental composition of multiphase metal chalcogenide thin films deposited at electrodeposition potentials of (a) 4V, (b) 6 V, (c) 8 V, and (d) 10 V.

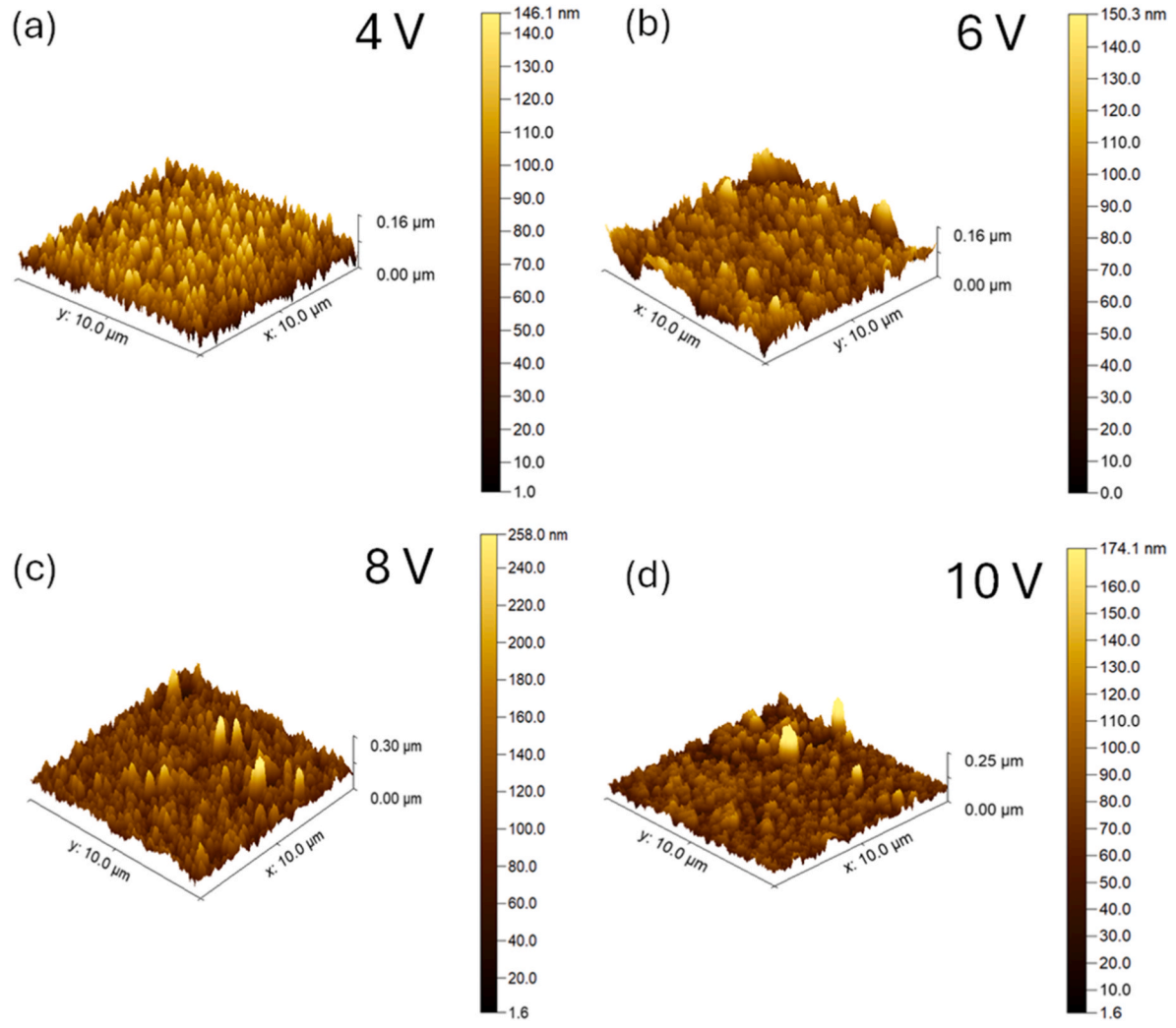

Fig. 8. 3-D AFM images of multiphase metal chalcogenide thin films deposited at electrodeposition potentials of (a) 4V, (b) 6 V, (c) 8 V, and (d) 10 V.

Table 2
Topographical parameters extracted from HR-AFM of metal chalcogenide thin films synthesized by various electrodeposited potentials.

Applied potentials	Surface slope, S_{dq}	Mean roughness, S_a (nm)	RMS roughness, S_q (nm)	$RMS = \sqrt{S_a^2 + S_q^2}$ (nm)
4 V	0.3652	16.6455	20.8373	26.6696
6 V	0.2784	15.0136	18.9555	24.1810
8 V	0.4154	20.7929	28.0632	34.9269
10 V	0.3260	16.2566	22.2768	27.5778

applications [37].

3.4. X-ray photoelectron spectroscopy (XPS)

The XPS survey scan (Fig. 9(a)) of the sample reveals peaks of C 1s, Bi 4f, Te 3d, Al 2s/Al sp, Sn 3d, and O 1s + Sb 3d. The presence of the O 1s peak indicates that oxidation of the thin film occurred upon exposure to the atmosphere. The high-resolution spectrum for the three set of doublets with the spin-orbit splitting separation (~5.3 eV) of Bi 4f in Fig. 9 (b) shows the strong Bi $4f_{5/2}$ and Bi $4f_{7/2}$ peaks at 159.1 and 164.4 eV, respectively, which are attributed to Bi^{3+}. These strong peaks can be subdivided into three distinct peaks. Among them, the peaks centered at 160.1 eV and 165.4 eV are also attributed to Bi^{3+} in the thin film, while the rest peaks centered at 157.5 eV and 162.8 eV belong to metallic Bi^0 [38]. For the analysis of the Te 3d peaks in Fig. 9(c), four sets of doublets with spin-orbit splitting separation (~10.4 eV) were used. The strong peaks are located at 576.1 eV ($3d_{5/2}$) and 586.5 eV ($3d_{3/2}$) with the B 4f states indicate the presence of surface oxide on Bi_2Te_3 nanostructures and can be formed to $Bi_xTe_xO_z$ [39]. Other three peaks, exhibited at 572.8 eV for Te $3d_{5/2}$ and 583.2 eV for Te $3d_{3/2}$ indicate that the Te species oxidized from Te to Te^{2-} to form TeO_2 in the film, which is consistent with the typical binding energies of metal tellurides for Bi–Te systems, that is, most Bi_2Te_3 compounds [39]. For the peaks at 574.1 and 584.5 eV can be attributed to the elemental tellurium (Te^0) and indicated to the presence of unoxidized Te in the thin film [40]. Other peaks at the higher binding energy of 577.4 and 587.9 eV correspond to Te^{4+} oxidation states, corresponding to the presence of oxidized tellurium species, such as TeO_2, on the surface of the sample [41]. The peak for Al 2p (Fig. 9(d)) can be deconvoluted into two peaks of γ-Al_2O_3 and AlOOH or $Al(OH)_3$ at 74.7 and 76.3 eV respectively, which is the coexistence of oxide and hydroxide phases of aluminum on the surface [42]. In our results, there was no observed anhydride Al_2O_3 peak in the spectrum. This indicates that Al_2O_3 corresponds to hydroxyl groups during thin film synthesis. However, another Al 2s state was observed at the low-intensity peak ~ at 119 eV, as shown in Fig. 9(e). This also indicates the presence of Al^{3+} species, which are typically associated with aluminum oxide (Al_2O_3) [43]. In Fig. 9(f), the main peak of XPS spectrum for O 1s at 530.7 eV is ascribed to lattice oxygen or the presence of O^{2-} ions in oxygen-deficient regions in the thin film, whereas the peak at

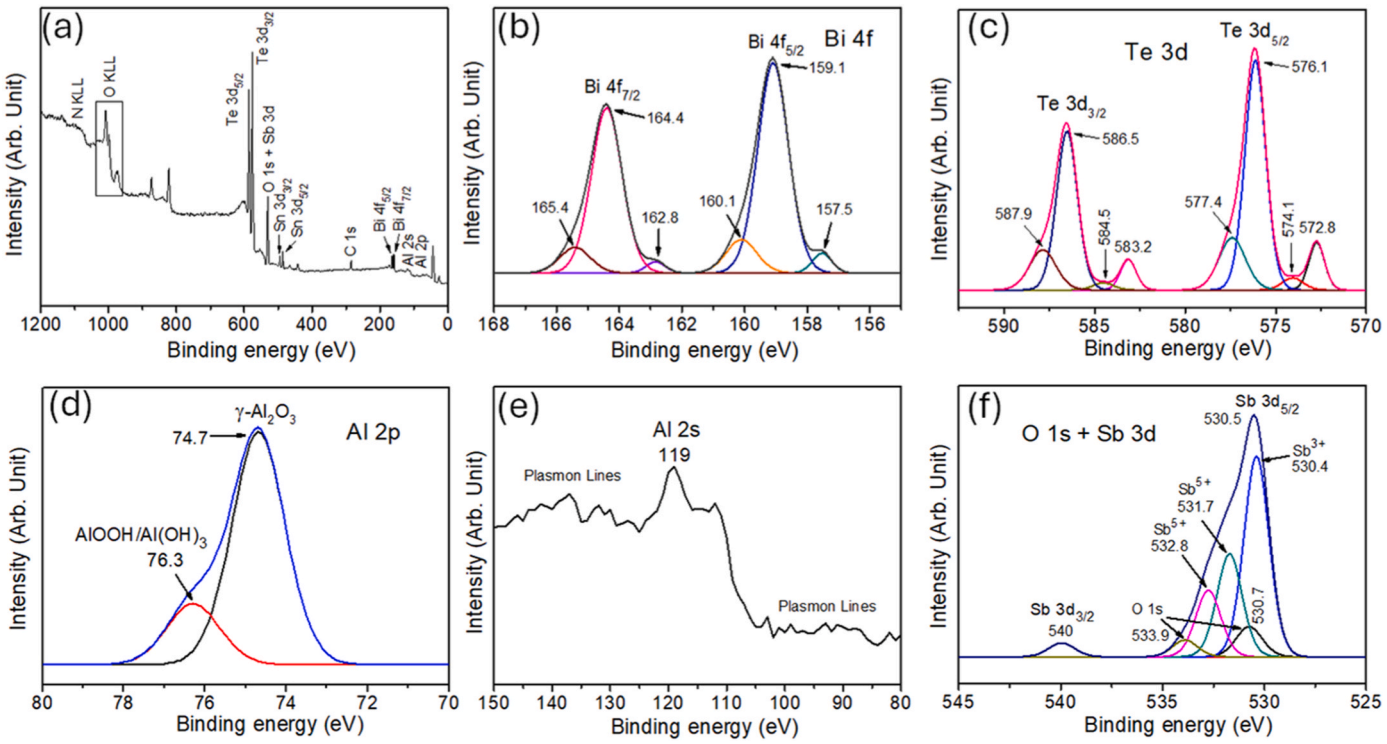

Fig. 9. X-ray photoelectron spectroscopy (XPS) for (a) Survey spectrum, (b) Bi 4f, (c) Te 3d, (d) Al 2p, (e) Al 2s, and (f) O1s + Sb 3d.

533.9 eV is associated with oxygen or hydroxyl (OH) species chemically absorbed or dissociated at the sample surface, such as adsorbed H_2O [44]. The spin–orbit coupling of the Sb 3d state with a spin–orbit separation of 9.5 eV, which agrees well with that reported previously for Sb_2O_3 [45]. The deconvoluted XPS peak in the Sb $3d_{5/2}$ region can be observed at 530.4 eV is assigned to lattice oxygen (Sb–O) generated during air exposure and corresponds to the chemical state of Sb^{3+} for antimony in the Sb_2O_3 compound [46], while the higher binding energy peaks at ~531.7 and ~532.8 eV correspond to the Sb^{5+} state with lattice oxygen in Sb_2O_3 and surface hydroxyl groups or adsorbed oxygen species. Furthermore, a peak in the Sb $3d_{3/2}$ region centered around 540 eV was observed due to Sb^{3+} forming Sb_2O_3 and Sb^{5+} to form Sb_2O_5 in the thin film [47,48]. The presence of Sb_2O_3 and Sb_2O_5 implies that the thin film might have incorporated SbO, which contains a considerable

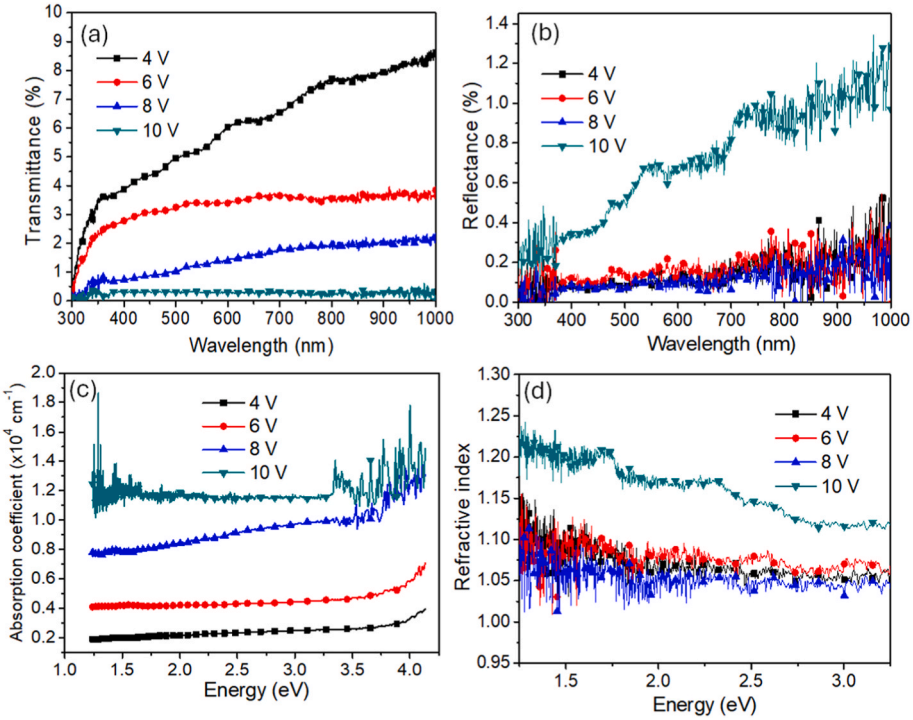

Fig. 10. (a) Transmittance, (b) reflectance, (c) absorption coefficient, and (d) refractive index of thin films deposited at various electrodeposition potentials.

quantity of Sb_2 although this compound cannot be detected in the XRD pattern [49].

3.5. Optical properties

Fig. 10(a) displays the transmittance spectra of the multiphase metal chalcogenide thin films deposited at different applied electrodeposition potentials. The average transmittance values in the wavelength range of 300–1000 nm were 6.017, 3.262, 1.452, and 0.280 % for applied potentials of 4, 6, 8, and 10 V, respectively. The corresponding reflectance spectra, displayed in Fig. 10(b), exhibited average values of 0.144, 0.164, 0.113, and 0.718 %, respectively. Although a slight reduction in reflectance was observed at 8 V, a pronounced increase occurred at 10 V. Despite the reduction in the film thickness at higher applied potentials, the transmittance decreased while the reflectance increased, which was attributed to the enhanced defect density and reduced crystallinity, ultimately approaching a quasi-crystalline structure. Additionally, the presence of cracks and the reduction in particle size enhance light scattering within the thin films, introducing additional scattering centers that reduce optical transmittance [50]. Furthermore, Alsulami et al. [51]. attributed a similar behavior to the increased free-carrier concentration within thin films. In this context, the Sb^3 + and Al^{3+} ions act as acceptor dopants, generating holes in the valence band. According to the Drude model of optical conductivity, these free carriers absorb photon energy through intraband transitions, thereby enhancing surface reflectivity. Additionally, Fig. 10(c) shows that the absorption coefficient increases with increasing applied electrodeposition potential. This enhancement is attributed to co-doping within the Bi_2Te_3 lattice, which introduces intermediate energy levels within the band gap and facilitates sub-band-gap optical transitions. As a result, a greater number of incident photons are absorbed within the thin film, with most of the energy carried by the photons being dissipated near the film surface [52]. This process promotes electron excitation from the valence band to the conduction band, thereby reducing optical transmittance [53]. The present observations are consistent with previous reports on potassium (K)-doped manganese vanadium oxide (Mn_2VO_4) [54] and K-doped vanadium oxide (V_2O_5) thin films [52].

The electronic polarizability of ions and the local field within thin films are directly related to the optical refractive index *(n)*, which is important for characterizing optical materials. The refractive index indicates the speed at which light propagates through a material and governs a wide range of linear and nonlinear optical phenomena, including dielectric constants, optoelectrical conductivity, electronegativity, first- and third-order susceptibilities, and nonlinear refractive index for photocatalytic activity and various optoelectronic applications [27], [55]. The refractive indices of the multiphase metal chalcogenide thin films were estimated using Eq. (4) [34], [55], [56]:

$$n = \left(\frac{1+R}{1-R}\right) + \sqrt{\frac{4R}{(1-R)^2} - k^2} \tag{4}$$

Fig. 10(d) illustrates the refractive index variation as a function of the photon energy. As observed, the refractive index was high in the near-infrared region and decreased linearly toward the UV region. The average refractive index values were 1.076, 1.080, 1.055, and 1.170 for the applied potentials of 4, 6, 8, and 10 V, respectively. This variation in the refractive index can be attributed to successive internal reflection and various excitations occurring within the films [34]. The refractive index is influenced by multiple factors, including the material density, crystal structure, and surface compositional profile of thin films [57]. The highest refractive index was obtained for the thin film deposited at 10 V, which can be attributed to the enhanced density, formation of optically dense nanostructures, and enhanced light scattering associated with the crack-induced surface morphology. Despite the presence of such defects, a high refractive index remains a desirable attribute for photonic materials, making these multiphase metal chalcogenide thin films attractive for optoelectronic applications such as solar cells, Bragg reflectors, and optical sensors [57].

The band gap (E_g) is a key parameter for evaluating thin-film semiconductor–based devices and was determined from the absorption coefficient using the Tauc formula [55], [56]:

$$\alpha h\nu = K\left(h\nu - E_g\right)^m \tag{5}$$

where K is a constant related to the optical transition type and is dependent on the electron–hole mobility, h is Planck's constant (4.135×10^{-15} eV s), $h\nu$ is the photon energy interacting with the material, and m is an index associated with the nature of the interband transition. It is known that these two types (direct or indirect) of band gaps are theoretically different, especially in pure substances, and under certain conditions, only one type of a direct band gap can be existed in a compound. However, in Fig. 11(a) and (b), we choose to divide the presentation from optical characterization investigated by UV-Vis spectroscopy into direct and indirect features, where these data come from measurements of multiatom-doped thin films. The value of m equals 1/2 and 2 for the allowed direct and indirect bandgap transitions, respectively. The bandgap (E_g) was determined by extrapolating the intercept of the linear fit on the x-axis at $(\alpha h\nu)^2 = 0$ or $(\alpha h\nu)^{1/2} = 0$. As shown in Fig. 11(a), the direct band gap was observed decreasing from 3.75 to 1.52 eV with increasing applied electrodeposition potentials. While the indirect band gap values (Fig. 11(b)) ranged from 2.90 to 0.25 eV. The observed decrease in E_g is accompanied by a red shift at higher applied potentials, which is associated with changes in carrier concentration induced by the substitution of Sb^{3+} and Al^{3+} ions into the Bi_2Te_3 lattice. This behavior can be discussed in the context of the Burstein–Moss effect, which reflects the modification of the electronic band structure with increasing dopant-induced carrier density. The incorporation of Sb^{3+} and Al^{3+} ions introduced impurity band levels within the bandgap of Bi_2Te_3. These additional states, arising from the synergistic effect of Sb^{3+} and Al^{3+} ions, provide electronic levels that require a lower excitation energy for electrons to reach the conduction band edge, thereby effectively narrowing the energy band gap [56], [58], [59].

In addition, the substitution of Sb^{3+} and Al^{3+} ions into Bi_2Te_3 promotes the transition of electrons from the filled valence band to defect-related recombination centers rather than directly to the empty conduction band. The improved electron-phonon interaction at higher applied electrodeposition potentials alters the lattice parameters by increasing the dislocation density, microstrain, and lattice disorder, thereby altering the crystallinity of the multiphase metal chalcogenide films. These structural changes play a key role in modulating the optical behavior of multiphase metal chalcogenide films, particularly contributing to bandgap reduction [18], [53].

The significant reduction in the optical band gap at higher applied potential is attributed to Several concurrent effects were observed: (1) the high deposition potential (10 V) likely introduces a high density of structural defects, such as vacancies, interstitials, and disordered regions. These defects create localized states near the band edges, effectively narrowing the apparent optical band gap; (2) at elevated electrodeposited potentials, rapid nucleation and growth can lead to poor crystallinity or partial amorphization, which promote band tail-state formation and are known to reduce the optical band gap due to band edge smearing; (3) the increase in carrier concentration due to defect states or doping-like effects can lead to many-body interactions that reduce the effective band gap; and (4) a high electrodeposited potential may induce non-stoichiometric or multiphase phases, which can possess intrinsically lower band gaps [60–63].

Although the band gap (~0.25 eV) is unusually low for conventional optoelectronic applications, it has several important implications in the mid-to far-infrared region with more effective utilization of a broad solar photon spectrum, thereby strengthening optical absorption at lower photon energies and shifting the effective absorption edge toward the near-infrared (NIR) region, which is advantageous for solar cell

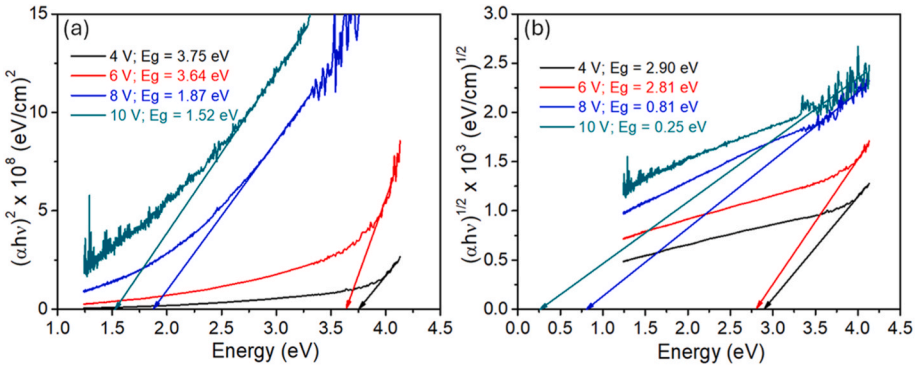

Fig. 11. Tauc plot analysis for determination of thin films deposited at various electrodeposition potentials, which are classified as (a) direct band gap and (b) indirect band gap.

applications [64] and may be useful for IR detectors, thermal sensing applications, and photothermal conversion systems [65,66]. In terms of increased carrier concentration and enhanced electrical conductivity, a reduced bandgap is typically beneficial for electrochemical electrodes, charge transport layers, and energy storage devices [67].

3.6. Electrical properties

The temperature-dependent DC conductivity (σ_{dc}) of the multiphase metal telluride thin films deposited at different applied electrodeposition potentials was analyzed to elucidate the thermally activated charge-transport mechanism using the Arrhenius relation [52], [68]:

$$\sigma_{dc} = \sigma_0 \, exp\left(\frac{-E_{ac}}{K_B T}\right) . \quad (6)$$

where K_B denotes the Boltzmann constant (8.617×10^{-5} eV/K), σ_o represents the pre-exponential factor, and $-E_{ac}$ represents the activation energy of the thin films deposited at different applied electrodeposition potentials.

Fig. 12(a–d) depict the Arrhenius plots (ln σ vs. 1000/T) for the multiphase metal telluride thin films deposited at different applied electrodeposition potentials. The linear behavior of these plots shows the characteristics of semiconducting materials and indicates an enhanced electrical conductivity with increasing temperature. The presence of a single linear regime in the Arrhenius plots suggested a dominant conduction mechanism throughout the measured temperature range. The thermal activation energy (E_{ac}) increased from 91.43 meV to 209.05 meV as the applied potential rose from 4 to 6 V, followed by a pronounced decrease to 61.78 meV for 8 V, and then increased again to 183.54 meV at 10 V. The significant decline in E_{ac} value between 6 and 8 V identifies this range as the optimal operating window, as it enables more efficient thermally activated conduction, which is particularly advantageous for device applications. The reduction in E_{ac} induced by Sb^{3+} and Al^{3+} co-doping during the growth process can be attributed to three synergistic mechanisms: (1) The introduction of additional charge carriers through the reduction of Bi^{3+} (trivalent bismuth) to Bi^{2+} (divalent bismuth), which lowers the energy barrier for charge transport. The Bi^{2+} state provides shallower electron traps or acts as an intermediate state for efficient charge transfer, thus increasing carrier

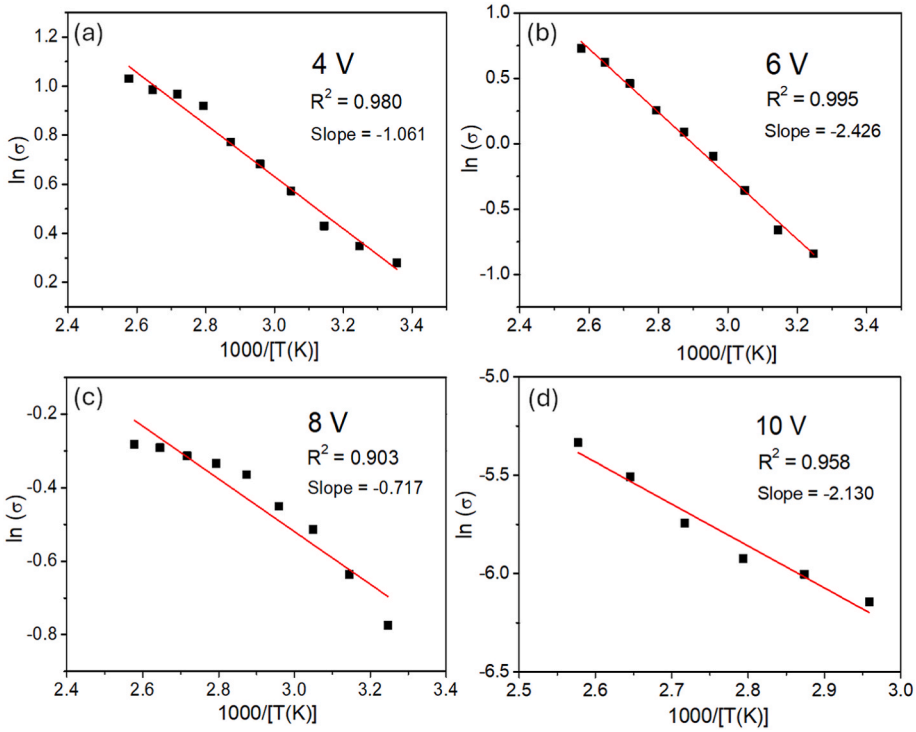

Fig. 12. Plots of ln (σ) vs. $1000/T(\mathrm{K})$ for electrodeposited-multiphase metal chalcogenide thin films used to determine the activation energy calculation.

mobility and electrical conductivity [69]. (2) The formation of defect-related localized states within the forbidden bandgap promotes hopping-assisted charge transport. At higher applied electrodeposition potentials, this favors a transition from band-like conduction to variable-range hopping–dominated transport, and (3) the increase in optimal grain boundary density associated with some crack formation in the thin films via a more continuous and compact morphology, which increases grain boundary scattering and alters the mobility-conductivity relationship, which results in a non-monotonic dependence of electrical conductivity on co-doping concentration and applied electrodeposition potential, where increased carrier concentration competes against reduced carrier mobility. Overall, the observed decrease in E_{ac} is consistent with previously reported results for K-doped V_2O_5 thin films and aligns well with the conduction mechanism proposed by Alsalme et al. [52]. However, a more pronounced surface cracking density appeared at 10 V, which led to an increase in the activation energy due to more crack edges acting as a potential barrier that introduced localized states and trap charges. Consequently, the thin film becomes electrically discontinuous; therefore, carriers must overcome higher barriers to move across the isolated regions. Thus, the high density of crack formation from a high electrodeposited potential is often associated with dangling bonds, vacancies, or disorder, introducing trap-assisted conduction mechanisms that require a higher activation energy.

Furthermore, the sheet resistance, resistivity, carrier concentration, conductivity, and mobility parameters are provided as a function of the applied electrodeposition potential and are important for identifying the optimum synthesis conditions for altering the physical properties of multiphase metal chalcogenide thin films. According to Hall effect measurements, n-type thin film semiconductors are also indicated for this type of metal chalcogenide thin film with the incorporation of Al^{3+} and Sb^{3+}. In Table 3, the decrease in sheet resistance and resistivity with increasing applied electrodeposited potential from 4 to 8 V mainly results from the increase in carrier concentration. With this applied electrodeposited potential range, the ions from the precursor solution and aluminum plate reached a higher kinetic energy to the conductive glass substrate, leading to increased local bonding order and fewer dangling bonds in the deposited films [70]. Consequently, it could be inferred that thin films with higher electrodeposited potential might also have a more ordered microstructure and fewer defects, thus resulting in lower resistivity and higher carrier concentration of thin films [71].

For the high applied electrodeposited potential of 10 V, slightly higher resistance, resistivity, and lower conductivity were obtained due to changes in the surface morphology and defect structure and related to changes in oxygen stoichiometry and defect chemistry as a result of stress relaxation [72,73]. Furthermore, it has been reported that microstructural changes with cracks and defect-induced scattering mechanisms affect the resistivity for a high applied electrodeposited potential [74,75]. The slight enhancement of the carrier concentration for this high applied potential might be attributed to the grain-boundary-dominated transport mechanisms in nanostructured thin films. Thus, the grain boundary and interface-related transport mechanisms can significantly influence the electrical behavior of lower-thickness thin films. In the case of the applied potential-dependent variation of electron mobility, the increase in mobility from an applied potential of 4 to 6 V demonstrates grain boundary scattering and crystal quality control of carrier transport in polycrystalline thin films. Mobility can then be improved when the grain boundary effects are reduced [76]. In polycrystalline films for applied potentials ranging from 8 to 10 V, mobility deteriorates at reduced thicknesses owing to the dominance of ionized impurity scattering and grain boundary scattering. Thus, the obtained multiphase chalcogenide thin film with optimal properties by a scalable technique paves the way for applications in plasmonic, optoelectronic devices, and thin-film solar cells [77].

3.7. Density functional theory (DFT) calculations

Density functional theory (DFT) calculations were employed to validate and benchmark the experimental observations. All the considered compounds were fully geometry-optimized, and their optical properties were systematically evaluated using *ab initio* methods. DFT calculations were performed using a plane-wave cutoff energy of 400 eV, with *k*-point sampling chosen to satisfy $1/k < 0.04$ in each crystallographic direction. Structural optimization and optical property calculations were performed within the generalized gradient approximation using the Perdew–Burke–Ernzerhof functional [78,79]. Bi_2Te_3 and Sb_2Te_3 crystallize in the rhombohedral space group *R-3m*, whereas Al_2Te_3 adopts the monoclinic $P2_1/c$. Al_7Te_{10} was identified as belonging to the rhombohedral *R32* space group. In addition, several Bi–Te secondary phases were detected, including BiTe (*P-3m1*), Bi_2Te (*P-3m1*), and Bi_4Te_3 (*R-3m*) (Fig. 13). As shown in Fig. 14, the photoabsorption coefficient (α) of the optimized structures was calculated from the imaginary part of the complex refractive index, which was directly related to the complex dielectric function ($\varepsilon = \varepsilon_1 + i\varepsilon_2$). The real ($\varepsilon_1$) and imaginary ($\varepsilon_2$) components of the dielectric function were evaluated using the matrix elements of the position operator, which describe the allowed electronic transitions within the material [80]. The photoabsorption coefficient presented in Fig. 14(a) shows that the well-established compounds Bi_2Te_3 and Sb_2Te_3 exhibit significantly higher absorption coefficients than those of Al_2Te_3 and Al_7Te_{10}. In contrast, a comparison of the different Bi–Te compositions in Fig. 14(b) reveals that Bi_2Te_3 delivers the highest absorption coefficient in the high-photon energy region, whereas the other Bi–Te phases exhibit stronger absorption, predominantly in the red (low-energy) region.

4. Conclusions

In this study, the influence of applied electrodeposition potentials on the physical properties of multiphase metal telluride thin films are systematically demonstrated, highlighting their suitability for a range of optoelectronic applications. XRD analysis confirmed the formation of rhombohedral Sb_2Te_3, Bi_2Te_3, Al_7Te_{10}, and Bi_4Te_3 phases, which were incorporated into the thin films alongside hexagonal Bi_2Te, BiTe, and monoclinic Al_2Te_3. These phases arise from the co-doping of Sb^{3+} and Al^{3+} ions into the Bi_2Te_3 solution and the use of an aluminum plate, respectively. The complementary EDS spectra further confirmed the compositional variations consistent with the co-doping of Sb^{3+} and Al^{3+} ions. The optical characterization investigated by UV-Vis spectroscopy of the dopant thin films, which are classified into direct and indirect band gaps. It revealed a progressive reduction in both direct and indirect band gaps, decreasing from 3.75 to 1.52 eV and from 2.90 to 0.25 eV, respectively. This trend is consistent with the Burstein-Moss effect and indicates an increase in carrier concentration. Furthermore, substitution of Sb^{3+} and Al^{3+} ions into Bi_2Te_3 improved the electron-phonon

Table 3
Electrical parameters extracted from Van der Pauw Hall effect measurement.

Applied potentials	Sheet resistance (Ω)	Resistivity (Ω·cm)	Carrier concentration (cm^{-3})	Conductivity $(\Omega\cdot cm)^{-1}$	Mobility ($cm^2/V\cdot s$)
4 V	1.67×10^4	21.7	9.837×10^{15}	0.0461	29.232
6 V	868.9	0.695	13.460×10^{15}	1.44	667.008
8 V	9.223	4.611×10^{-3}	3.246×10^{19}	217	41.697
10 V	10.38	5.191×10^{-3}	3.599×10^{19}	193	33.409

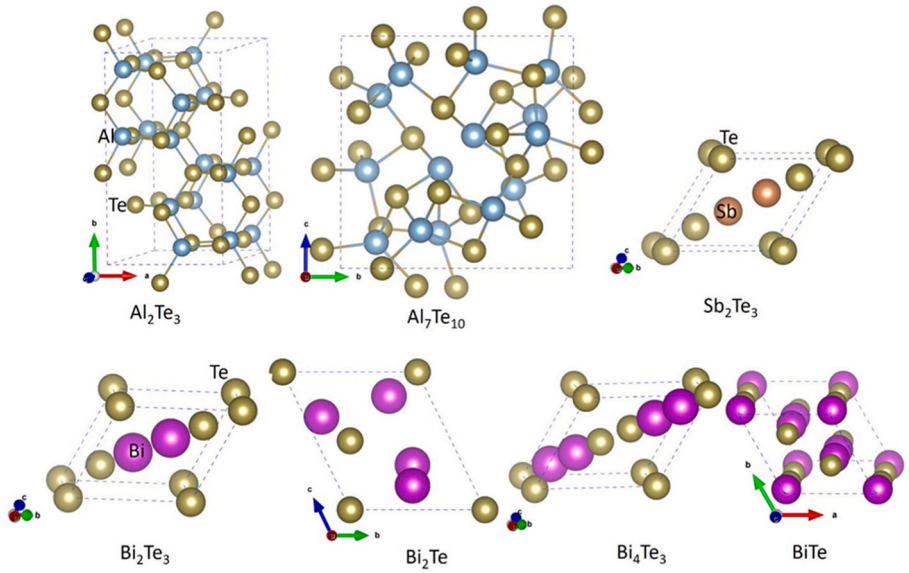

Fig. 13. Crystal structures of metal tellurides (Al, Bi, Sb) obtained using DFT calculations and compared with the experimental results.

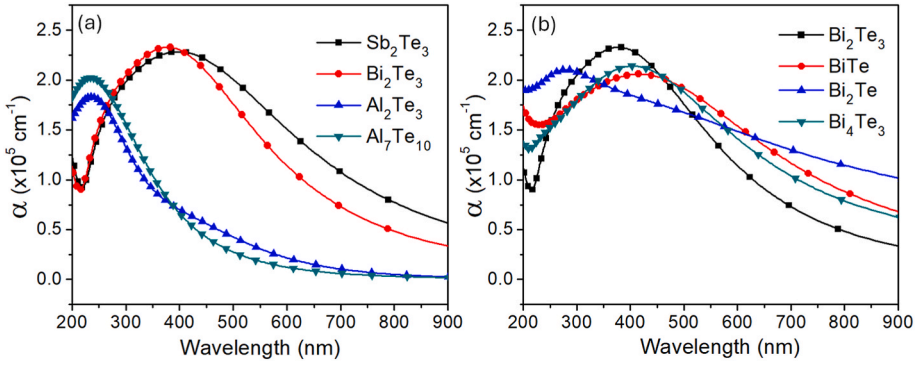

Fig. 14. Photoabsorption coefficients calculated from DFT.

interaction with increasing applied electrodeposition potential, inducing lattice parameter modification and improved crystallinity, which collectively contributed to the observed bandgap narrowing. Multiphase metal telluride thin films deposited at different electrodeposition potentials have tunable optical bandgaps and optical transparency. Films with wider band gaps showed high transparency, whereas those with narrower band gaps displayed enhanced solar spectrum absorption, making these materials strong candidates for a range of optoelectronic applications. Potential applications include window layers, photodiodes, buffer layers, transparent electrodes in heterostructured CIGS, and perovskite solar cells. These technological features make the films highly attractive for next-generation energy storage and linear/nonlinear optical sensing devices. Thus, the observed decrease in the band gap is suggestive of modifications in the electronic structure and improved crystallinity due to the increasing electrodeposition potential and greater incorporation of Sb^{3+} and Al^{3+} ions into the Bi_2Te_3 lattice. Moreover, the electrical properties were also altered in accordance with the type of dopants, incorporation mechanism, and oxygen vacancies under the applied electrodeposition potential. These issues have been found to play a significant role in thin-film synthesis. A pronounced decline in E_{ac} extracted from the Arrhenius plot, was observed between 6 V and 8 V. This behavior identifies this voltage window as the optimal applied potential for device applications, as it enables more efficient thermally activated conduction. Finally, DFT calculations revealed that Bi_2Te_3 and Sb_2Te_3 exhibit higher absorption coefficients than Al_2Te_3 and Al_7Te_{10}. Among these, Bi_2Te_3 demonstrated the strongest absorption at higher photon energies, whereas the remaining phases exhibited enhanced absorption predominantly in the red region of the spectrum.

CRediT authorship contribution statement

Panupat Chaiworn: Writing – original draft, Validation, Supervision, Methodology, Investigation, Funding acquisition, Data curation. **Pensri Pramukkul:** Writing – review & editing, Validation, Investigation, Data curation. **Prayoonsak Pluengphon:** Writing – original draft, Validation, Investigation, Data curation. **Ekasiddh Wongrat:** Writing – review & editing, Validation, Funding acquisition. **Phathaitep Raksa:** Writing – review & editing, Validation, Investigation. **Piyanooch Nedkun:** Writing – review & editing, Validation, Investigation. **Auttasit Tubtimtae:** Writing – original draft, Validation, Supervision, Methodology, Formal analysis, Conceptualization.

Ethical approval

This study was conducted in full compliance with established ethical standards.

Declaration of competing interest

The authors declare that they have no known competing financial interests or personal relationships that could have appeared to influence the work reported in this paper.

Acknowledgments

The authors gratefully acknowledge financial support provided by the Department of Physics and General Science, Faculty of Science and Technology, Chiang Mai Rajabhat University (Grant No. CMRU 30/66). This work was partially supported by computer simulations from the Huachiew Chalermprakiet University and the Fundamental Fund (2026). Additional support from the University of Phayao and the Thailand Science Research & Innovation Fund (Fundamental Fund 2026, Grant No. 2261) is acknowledged. This paper was proofread and edited by Editage Singapore through the Paperpal of Cactus Communications Services Pte Ltd.

Data availability

All data supporting the findings of this study are included within the article

References

[1] M.M. Abdelrazek, M.E. Abd-Elrazek, D.E. El Refaay, M.M. El-Desoky, Enhanced optical properties of V_2O_5 thin films through rare earth co-doping for optoelectronic applications, Physica B 699 (2025) 416881, https://doi.org/10.1016/j.physb.2024.416881.

[2] A.S. Najm, H.S. Naeem, D.A.R.M. Alwarid, A. Aljuhani, S.A. Hasbullah, H.A. Hasan, K. Sopian, B. Bais, H.J. Al-Iessa, H.Sh Majdi, A.J. Sultan, H. Moria, Mechanism of chemical bath deposition of CdS thin films: influence of sulphur precursor concentration on microstructural and optoelectronic characterizations, Coatings 12 (2022) 1400, https://doi.org/10.3390/coatings12101400.

[3] H. Kafashan, Z. Orshesh, A. Bahrami, F. Zakerian, Structural and optoelectronic properties of electrodeposited CdSe thin films: effect of Cu-dopant, Physica B 675 (2024) 415623, https://doi.org/10.1016/j.physb.2023.415623.

[4] A.Z. Arsad, M.S. Bahrudin, N.A. Arzaee, Mohd Nazri Abd Rahman, C.F. Chau, S. F. Abdullah, A.W. Mahmood Zuhdi, Zinc sulfide thin films deposited by chemical bath: tuning consideration of structural, optical band gap, and electrical properties for CIGS solar cells application, Ceram. Int. 50 (2024) 11776–11786, https://doi.org/10.1016/j.ceramint.2024.01.082.

[5] J.T. Harrison, M.C. Gupta, Photoconductive PbSe thin films and the role of potassium iodide, J. Alloys Compd. 905 (2022) 164155, https://doi.org/10.1016/j.jallcom.2022.164155.

[6] X. Ai, S. Yan, Y. Chen, S. Chen, Y. Jiang, X. Song, L. Ma, X. Wu, Microstructure and optical properties of CdTe thin films prepared by close spaced sublimation method at various growth temperatures, J. Lumin. 252 (2022) 119372, https://doi.org/10.1016/j.jlumin.2022.119372.

[7] J. Park, J. Seo, J.-H. Lim, B. Yoo, Synthesis of copper telluride thin films by electrodeposition and their electrical and thermoelectric properties, Front. Chem. 10 (2022) 799305, https://doi.org/10.3389/fchem.2022.799305.

[8] D.S. Cuz, M. De La Luz Olvera Amador, S.D.C. Quiñones, F.J. De Moure Flores, J. S. Cruz, Structural, optical and morphological characterization of Sb_2S_3 thin films grown by physical vapor deposition, in: Proceedings of the 2021 18th International Conference on Electrical Engineering, Computing Science and Automatic Control (CCE), Mexico City, Mexico,, 2021, pp. 1–5, https://doi.org/10.1109/CCE53527.2021.9633025.

[9] P. Ilaiyaraja, V. Sharma, A.C. Dakshinamurthy, T.K. Das, C. Sudakar, Fabrication of metal chalcogenide thin films by a facile thermolysis process under air ambient using metal-3-mercaptopropionic acid complex, Mater. Res. Bull. 141 (2021) 111346, https://doi.org/10.1016/j.materresbull.2021.111346.

[10] A. Sabzalipour, M. Mir, M. Zarenia, B. Partoens, Two distinctive regimes in the charge transport of a magnetic topological ultra thin film, New J. Phys. 22 (2020) 123004, https://doi.org/10.1088/1367-2630/abc989.

[11] J. Bibby, A. Singh, E. Heppell, J. Bollard, B. Achinuq, S.J. Haigh, G. van der Laan, T. Hesjedal, Synthesis of nanocrystalline Mn-doped Bi_2Te_3 thin films via magnetron sputtering, Crystals 15 (2025) 54, https://doi.org/10.3390/cryst15010054.

[12] M.-K. Han, H. Ryu, S.-J. Kim, Effect of chromium doping on the thermoelectric properties of Bi_2Te_3: $Cr_xBi_2Te_3$ and $Cr_xBi_{2x}Te_3$, J. Electron. Mater. 42 (9) (2013) 2612–2619, https://doi.org/10.1007/s11664-013-2670-4.

[13] J. An, M.-K. Han, S.-J. Kim, Synthesis of heavily Cu-doped Bi_2Te_3 nanoparticles and their thermoelectric properties, J. Solid State Chem. 270 (2019) 407–412, https://doi.org/10.1016/j.jssc.2018.11.024.

[14] X. Guo, J. Qin, X. Lv, L. Deng, X. Jia, H. Ma, H. Jia, Effect of doped indium into Bi_2Te_3 matrix on the microstructure and thermoelectric transport properties, RSC Adv. 6 (2016) 60736–60740, https://doi.org/10.1039/C6RA09767G.

[15] A.A. Belik, W. Yi, High-pressure synthesis, crystal chemistry and physics of perovskites with small cations at the A site, J. Phys. Condens. Matter 26 (2014) 163201, https://doi.org/10.1088/0953-8984/26/16/163201.

[16] H. Li, P.J. Sadler, H. Sun, Unexpectedly strong binding of a large metal ion (Bi^{3+}) to human serum transferrin, J. Biol. Chem. 271 (1996) 9483–9489, https://doi.org/10.1074/jbc.271.16.9483.

[17] V. Jović, Tellurium, in: Geochemistry, Encyclopedia of Earth Science, Springer, Dordrecht, 1998, https://doi.org/10.1007/1-4020-4496-8_316.

[18] T. Çayır Taşdemirci, SILAR growth of pure CdO and copper-doped CdO thin films: structural, optical and electrical properties, Mater. Chem. Phys. 346 (2025) 131320, https://doi.org/10.1016/j.matchemphys.2025.131320.

[19] E.R. Leite, M.I.B. Bernardi, E. Longo, J.A. Varela, C.A. Paskocimas, Enhanced electrical property of nanostructured Sb-doped SnO_2 thin film processed by soft chemical method, Thin Solid Films 449 (2004) 67–72, https://doi.org/10.1016/j.tsf.2003.10.101.

[20] H. Li, L. Tian, Q. Yang, N. Wang, X. Fu, L. Zhou, J. Feng, H. Zhang, Sb^{3+} doped Cs_3YCl_6 metal halides with highly efficient broad-band green emission for light-emitting diode and X-ray imaging, Sci. China Mater. 68 (2025) 2459–2466, https://doi.org/10.1007/s11426-024-2674-7.

[21] A.M. Bolbol, H. Elshimy, O.H. Abd-Elkader, M. Kamel, S.A. Shata, N.Y. Mostafa, Impact of Sb-insertion on structural, optical, and dielectric characteristics of the PbI_2 thin film, Opt. Mater. 134 (2022) 113180, https://doi.org/10.1016/j.optmat.2022.113180.

[22] C. O'Rourke, D.R. Bowler, Intrinsic oxygen vacancy and extrinsic aluminum dopant interplay: a route to the restoration of defective TiO_2, J. Phys. Chem. C 118 (2014) 7261–7271, https://doi.org/10.1021/jp407736f.

[23] Q.C. Bui, V. Consonni, S. Boubenia, G. Gay, C. Perret, M. Zeghouane, S. Labau, H. Roussel, X. Mescot, G. Ardila, B. Salem, High figure-of-merit in Al-doped ZnO thin films grown by ALD through the Al content adjustment, Materialia 31 (2023) 101863, https://doi.org/10.1016/j.mtla.2023.101863.

[24] S. Gahlawat, J. Singh, A.K. Yadav, P.P. Ingole, Exploring Burstein–Moss type effects in nickel doped hematite dendrite nanostructures for enhanced photo-electrochemical water splitting, Phys. Chem. Chem. Phys. 21 (2019) 20463–20477, https://doi.org/10.1039/C9CP04132J.

[25] Q. Wang, M. Brier, S. Joshi, A. Puntambekar, V. Chakrapani, Defect-induced Burstein–Moss shift in reduced V_2O_5 nanostructures, Phys. Rev. B 94 (2016) 245305, https://doi.org/10.1103/PhysRevB.94.245305.

[26] K. Koonrungsesomboon, D. Boonyawan, K. Suttiat, P. Yavirach, Effect of immersion time in simulated body fluid on adhesion strength of hydrothermally treated hydroxyapatite–titanium nitride films on polyetheretherketones, CMU J. Nat. Sci. 21 (3) (2022) e2022042, https://doi.org/10.12982/CMUJNS.2022.042.

[27] J.O. Emegha, A. El-Rayyes, Y.S. Itas, M.U. Khandaker, The impact of iron concentration on the structural and optical properties of iron lead sulphide thin films, J. Indian Chem. Soc. 102 (2025) 102085, https://doi.org/10.1016/j.jics.2025.102085.

[28] M. Taoufiq, A. Soussi, A. Ait Hssi, S. Baoubih, A. Elfanaoui, Theoretical DFT and experimental investigation of the effect of Co doping in electrochemically deposited ZnSe films, Opt. Mater. 155 (2024) 115893, https://doi.org/10.1016/j.optmat.2024.115893.

[29] W. Qin, T. Nagase, Y. Umakoshi, J.A. Szpunar, Relationship between microstrain and lattice parameter change in nanocrystalline materials, Philos. Mag. Lett. 88 (2008) 169–179, https://doi.org/10.1080/09500830701840155.

[30] S. Mustapha, M.M. Ndamitso, A.S. Abdulkareem, J.O. Tijani, D.T. Shuaib, A. K. Mohammed, A. Sumaila, Comparative study of crystallite size using Williamson–hall and debye–scherrer plots for ZnO nanoparticles, Adv. Nat. Sci. Nanosci. Nanotechnol. 10 (2019) 045013, https://doi.org/10.1088/2043-6254/ab52f7.

[31] S. Jeon, X. Liu, C. Azersky, J. Ren, S. Zhang, W. Chen, R.W. Hyers, K. Costa, M. Kolbe, D.M. Matson, Particle size effects on dislocation density, microstructure, and phase transformation for high-entropy alloy powders, Materialia 18 (2021) 101161, https://doi.org/10.1016/j.mtla.2021.101161.

[32] Y. Han, Z. Liu, L. Guo, W. Wang, J.-G. Guo, Si-doping-induced reversal of surface energies in nonpolar (1010) and (1120) planes of AlN crystal, Surf. Interfaces 76 (2025) 107983, https://doi.org/10.1016/j.surfin.2025.107983.

[33] M.S. Sultan, Effect of surface morphology and elemental composition on the magnetization behaviour of electrodeposited NiFe films, J. Nanotechnol. 2024 (2024) 9310012, https://doi.org/10.1155/2024/9310012.

[34] J.O. Emegha, K.E. Ukhurebor, U.O. Aigbe, B. Olofinjana, S.O. Azi, M.A. Eleruja, Effect of deposition temperature on the properties of copper–zinc sulphide thin films using mixed copper and zinc dithiocarbamate precursors, Gazi Univ. J. Sci. 35 (2022) 1556–1570, https://doi.org/10.35378/gujs.887025.

[35] T.K. Matabana, C.M. Muiva, L.K. Benjamin, M. Madhuku, T. Mosimanegape, C. B. Tabi, Effect of 3 MeV proton ion irradiation on optical properties of $Se_{70}Te_{20}Sn_{10}$ thin films for photonic applications, Phys. B Condens. Matter 700 (2025) 416930, https://doi.org/10.1016/j.physb.2025.416930.

[36] T.K. Matabana, C.M. Muiva, M. Madhuku, N. Mehta, L.K. Benjamin, T. Mosimanegape, D.P. Sebuso, C.B. Tabi, Tuning linear and nonlinear optical properties of $Se_{70}Te_{20}Sb_{10}$ thin films via 3 MeV proton irradiation for photonic applications, Mater. Sci. Semicond. Process. 201 (2026) 110040, https://doi.org/10.1016/j.mssp.2025.110040.

[37] T.K. Matabana, C.B. Tabi, M. Madhuku, D.P. Sebuso, C.M. Muiva, The impact of proton ion irradiation on $Se_{70}Te_{20}In_{10}$ thin films: Linear and non-linear optical properties for photonic applications, Phys. B Condens. Matter 696 (2025) 416663, https://doi.org/10.1016/j.physb.2024.416663.

[38] C. Wu, C. Zhou, Y. Chen, Z. Peng, J. Yang, Y. Zhang, Simple fabrication of visible light-responsive Bi–BiOBr/$BiPO_4$ heterostructure with enhanced photocatalytic

activity, J. Nanomater. 2021 (2021) 4835596, https://doi.org/10.1155/2021/4835596.
[39] S.M. Patil, S.R. Mane, R.M. Mane, S.S. Mali, P.S. Patil, P.N. Bhosale, Synthesis and X-ray photoelectron spectroscopy (XPS) and thermoelectric studies of ternary $Bi_2(Te_{0.5}Se_{0.5})_3$ mixed-metal chalcogenide thin films by the arrested precipitation technique, Can. J. Chem. 89 (2011) 1375–1381, https://doi.org/10.1139/V11-107.
[40] M.O. Reese, C.L. Perkins, J.M. Burst, S. Farrell, T.M. Barnes, S.W. Johnston, D. Kuciauskas, T.A. Gessert, W.K. Metzger, Intrinsic surface passivation of CdTe, J. Appl. Phys. 118 (2015) 155305, https://doi.org/10.1063/1.4933186.
[41] H. Kong, J.B. Yeo, H.Y. Lee, A study on the properties of tellurium-oxide thin films based on the variable sputtering gas ratio, J. Kor. Phys. Soc. 66 (2015) 1744–1749, https://doi.org/10.3938/jkps.66.1744.
[42] Y. Xiang, C. Zhou, E. Jia, W. Wang, Oxidation precursor dependence of atomic layer deposited Al_2O_3 films in a-Si:H(i)/Al_2O_3 surface passivation stacks, Nanoscale Res. Lett. 10 (2015) 137, https://doi.org/10.1186/s11671-015-0798-2.
[43] K. Ali, K.-H. Choi, J. Jo, Y.W. Lee, High rate roll-to-roll atmospheric atomic layer deposition of Al_2O_3 thin films towards gas diffusion barriers on polymers, Mater. Lett. 136 (2014) 90–94, https://doi.org/10.1016/j.matlet.2014.07.186.
[44] K.S. Sánchez-Zambrano, M. Hernández-Reséndiz, C. Gómez-Rodríguez, L. V. García-Quiñonez, J.A. Aguilar-Martínez, E.A. Rodríguez-Castellanos, L. F. Verdeja, D. Fernández-González, G.A. Castillo-Rodríguez, XPS study on calcining mixtures of brucite with titania, Materials 15 (9) (2022) 3117, https://doi.org/10.3390/ma15093117.
[45] Z. Deng, D. Chen, F. Tang, J. Ren, A.J. Muscat, Synthesis and purple-blue emission of antimony trioxide single-crystalline nanobelts with elliptical cross section, Nano Res. 2 (2009) 151–160, https://doi.org/10.1007/s12274-009-9014-y.
[46] I. Martini, E. Chevallay, V. Fedosseev, C. Hessler, H. Neupert, V. Nistor, M. Taborelli, Surface characterization at CERN of photocathodes for photoinjector applications, in: Proc. IPAC2015, Richmond, VA, USA, 2015.
[47] L. Tan, A. Tang, Y. Zou, M. Long, Y. Zhang, J. Ouyang, J. Chen, Sb_2Se_3 assembling Sb_2O_3@attapulgite as an emerging composite for catalytic hydrogenation of p-nitrophenol, Sci. Rep. 7 (2017) 3281, https://doi.org/10.1038/s41598-017-03281-z.
[48] J. Chen, Y. Shao, D. Li, An antimonate pyrochlore ($H_{1.23}Sr_{0.45}SbO_{3.48}$) for photocatalytic oxidation of benzene: effective oxygen usage and excellent activity, J. Mater. Chem. A 5 (2017) 937–941, https://doi.org/10.1039/C6TA08652G.
[49] P. Ekwere, M. Ndipingwi, C. Nolly, C. Ikpo, E. Iwuoha, Microwave synthesis of antimony oxide graphene nanoparticles – a new electrode material for supercapacitors, Nanoscale Adv. 5 (2023) 5137–5153, https://doi.org/10.1039/d3na00514c.
[50] A. Alsulami, Exploration of the impact of indium-doping on the microstructural, dispersion, linear, and nonlinear optical properties of the ZnS thin films, Physica B 710 (2025) 417271, https://doi.org/10.1016/j.physb.2025.417271.
[51] A. Alsulami, H.Y.S. Al-Zahrani, Preparation and characterization of innovative $VSbO_4$ thin films via nebulized spray pyrolysis technique, Opt. Quant. Electron. 55 (2023) 1191–1203, https://doi.org/10.1007/s11082-023-05486-1.
[52] A. Alsalme, A. Alsulami, Influence of potassium doping on the microstructural, electrical, and optical properties of V_2O_5 thin films prepared by nebulizer spray pyrolysis, Physica B 723 (2026) 418053, https://doi.org/10.1016/j.physb.2025.418053.
[53] M.R. Khanlary, E. Rahmani, Z. Pasalari, A. Reyhani, Post-annealing effect on the structural and optical properties of tungsten trioxide thin films prepared by thermal evaporation, Mater. Chem. Phys. 338 (2025) 130670, https://doi.org/10.1016/j.matchemphys.2025.130670.
[54] I.M. El Radaf, Investigation of the effect of K-doping on the structural, dispersion, optical, and electrical properties of the Mn_2VO_4 thin films, J. Mater. Sci. Mater. Electron. 36 (2025) 1794–1803, https://doi.org/10.1007/s10854-025-15873-x.
[55] R. Özmenteş, A.S. Hassanien, Characterizations and optical discussions of thermally evaporated titanium dioxide thin films, J. Opt. 54 (2025) 1322–1340, https://doi.org/10.1007/s12596-024-02207-z.
[56] E. Elgazzar, Impact of Pd^{2+} and Sn^{4+} co-doping ZnO nanoflakes toward high-performing schottky diode based on the generation of intermediate bands within the energy gap, J. Mater. Sci. Mater. Electron. 35 (2024) 1697, https://doi.org/10.1007/s10854-024-13398-3.
[57] N. An, K. Wang, H. Wei, Q. Song, S. Xiao, Fabricating high refractive index titanium dioxide film using electron beam evaporation for all-dielectric metasurfaces, MRS Commun. 6 (2016) 77–83, https://doi.org/10.1557/mrc.2016.13.
[58] F.M. Hashem, E. Elgazzar, W.A. Mostafa, Ultrastructural changes in the fat body of desert locust, Schistocerca gregaria (Orthoptera: Acrididae) treated with zinc chromium oxide nanostructures via chemical co-precipitation approach, BMC Chem. 17 (2023) 7, https://doi.org/10.1186/s13065-023-00914-5.
[59] A.V. Babalola, V. Oluwasusi, V.A. Owoeye, J.O. Emegha, D.A. Pelemo, A.Y. Fasasi, U.M. Gurku, S.O. Alayande, S. Yusuf, B. Saje, Effect of tin concentrations on the elemental and optical properties of zinc oxide thin films, Heliyon 10 (2024) e23190, https://doi.org/10.1016/j.heliyon.2023.e23190.
[60] M. Qiu, Y. Xie, X. Gao, J. Li, Y. Deng, D. Guan, L. Ma, C. Yuan, Band gap opening and semiconductor–metal phase transition in (n,n) single-walled carbon nanotubes with distinctive boron–nitrogen line defect, Phys. Chem. Chem. Phys. 18 (2016) 4643–4651, https://doi.org/10.1039/C5CP06853C.
[61] C.-H. Ho, Amorphous effect on the advancing of wide-range absorption and structural-phase transition in γ-In_2Se_3 polycrystalline layers, Sci. Rep. 4 (2014) 4764, https://doi.org/10.1038/srep04764.
[62] A. Jain, P. Sagar, R.M. Mehra, Band gap widening and narrowing in moderately and heavily doped n-ZnO films, Solid State Electron. 50 (2006) 1420–1424, https://doi.org/10.1016/j.sse.2006.07.001.
[63] U. Prasad, P.R. Harsh, S.R. Kumar, K. Prasad, ZnTe thin films: deposition methods, physical properties, and device prospects, Int. J. Innov. Sci. Res. Technol. 11 (2026) 111, https://doi.org/10.38124/ijisrt/26feb111.
[64] T. Bhima Raju, B. Rajesh Kumar, Y. Ramakrishna, Effect of post-annealing temperature on microstructural, morphological and optical properties of sol–gel spin coated Cu doped SnO_2 thin films, Braz. J. Phys. 54 (2024) 238, https://doi.org/10.1007/s13538-024-01620-w.
[65] J. Wang, Y. Li, L. Deng, N. Wei, Y. Weng, S. Dong, D. Qi, J. Qiu, X. Chen, T. Wu, High-performance photothermal conversion of narrow-bandgap Ti_2O_3 nanoparticles, Adv. Mater. 29 (2017) 1603730, https://doi.org/10.1002/adma.201603730.
[66] Q.-Y. Chen, F.-J. Huang, J.-Q. Ruan, Y.-F. Zhao, X.-F. Zhang, K. Xiong, Y. He, CLEO collaboration, two-dimensional P3m1 Ca_3N_2, Ba_3P_2, and Ba_3As_2: promising stable narrow-gap semiconductors for infrared and broadband photodetectors, Phys. Rev. Appl. 22 (2024) 034013, https://doi.org/10.1103/PhysRevApplied.22.034013.
[67] B. Li, B. Luo, J. Zhao, Y. Pan, H. Zhou, Y. Xiao, S. Lei, B. Cheng, High electrical conductivity-induced enhancement effect of electrochemical performance in mesoporous $NiCo_2S_4$ nanorod-based supercapacitor, J. Energy Storage 26 (2019) 100955, https://doi.org/10.1016/j.est.2019.100955.
[68] A. Qasem, N.M. Said, A.A. Hassan, H.A. Yakout, E.R. Shaaban, Tunability of structural, optical, and electrical properties of pristine MnSe thin film by gradually changing temperature for optoelectronic applications, Physica B 627 (2022) 413600, https://doi.org/10.1016/j.physb.2021.413600.
[69] P. Dorenbos, Electronic structure of Bi-activated luminescent compounds and pure bismuth photocatalytic compounds, ECS J. Solid State Sci. Technol. 10 (2021) 086002, https://doi.org/10.1149/2162-8777/ac19c6.
[70] H.Q. Chiang, B.R. McFarlane, D. Hong, R.E. Presley, J.F. Wager, Processing effects on the stability of amorphous indium gallium zinc oxide thin-film transistors, J. Non-Cryst. Solids 354 (2008) 2826–2830, https://doi.org/10.1016/j.jnoncrysol.2007.10.105.
[71] J. Shi, C. Dong, W. Dai, J. Wu, Y. Chen, R. Zhan, The influence of RF power on the electrical properties of sputtered amorphous In–Ga–Zn–O thin films and devices, J. Semiconduct. 34 (2013) 084003, https://doi.org/10.1088/1674-4926/34/8/084003.
[72] E. Fortunato, P. Barquinha, R. Martins, Oxide semiconductor thin-film transistors: a review of recent advances, Adv. Mater. 24 (2012) 2945–2986, https://doi.org/10.1002/adma.201103228.
[73] J.H. Jeong, H.W. Yang, J.S. Park, J.K. Jeong, Y.-G. Mo, H.D. Kim, Origin of threshold voltage instability in amorphous indium–gallium–zinc oxide thin film transistors, Appl. Phys. Lett. 93 (2008) 123508, https://doi.org/10.1063/1.2990642.
[74] K. Iwaniak, W. Kaczorowski, B. Burnat, J. Grabarczyk, Impact of the applied electrode system on properties of electrodeposited calcium phosphate coatings, Mater. Sci. 18 (2025) 539, https://doi.org/10.3390/ma18030539.
[75] B.G. Tóth, L. Péter, Á. Révész, J. Pádár, I. Bakonyi, Temperature dependence of the electrical resistivity and the anisotropic magnetoresistance (AMR) of electrodeposited Ni–Co alloys, Eur. Phys. J. B 75 (2010) 167–177, https://doi.org/10.48550/arXiv.1607.01960.
[76] Y. Magari, W. Yeh, T. Ina, M. Furuta, Influence of grain boundary scattering on the field-effect mobility of solid-phase crystallized hydrogenated polycrystalline In_2O_3 (In_2O_3:H), Nanomaterials 12 (2022) 2958, https://doi.org/10.3390/nano12172958.
[77] R. Magrin Maffei, A. di Bona, M. Sygletou, F. Bisio, S. D'Addato, S. Benedetti, Suppression of grain boundary contributions on carrier mobility in thin Al-doped ZnO epitaxial films, Appl. Surf. Sci. 624 (2023) 157133, https://doi.org/10.1016/j.apsusc.2023.157133.
[78] J.P. Perdew, J.A. Chevary, S.H. Vosko, K.A. Jackson, M.R. Pederson, D.J. Singh, C. Fiolhais, Atoms, molecules, solids, and surfaces: applications of the generalized gradient approximation for exchange and correlation, Phys. Rev. B 46 (1992) 6671–6687, https://doi.org/10.1103/PhysRevB.46.6671.
[79] J.P. Perdew, K. Burke, M. Ernzerhof, Generalized gradient approximation made simple, Phys. Rev. Lett. 77 (1996) 3865–3868, https://doi.org/10.1103/PhysRevLett.77.3865.
[80] M.D. Segall, P.L.D. Lindan, M.J. Probert, C.J. Pickard, P.J. Hasnip, S.J. Clark, M. C. Payne, First-principles simulation: ideas, illustrations and the CASTEP code, J. Phys. Condens. Matter 14 (2002) 2717–2744, https://doi.org/10.1088/0953-8984/14/11/301.